Fully coupled approach to modeling shallow water flow, sediment transport, and bed evolution in rivers

Shuangcai Li[1] and Christopher J. Duffy[1]

Received 12 July 2010; revised 6 December 2010; accepted 21 December 2010; published 2 March 2011.

[1] Our ability to predict complex environmental fluid flow and transport hinges on accurate and efficient simulations of multiple physical phenomenon operating simultaneously over a wide range of spatial and temporal scales, including overbank floods, coastal storm surge events, drying and wetting bed conditions, and simultaneous bed form evolution. This research implements a fully coupled strategy for solving shallow water hydrodynamics, sediment transport, and morphological bed evolution in rivers and floodplains (PIHM_Hydro) and applies the model to field and laboratory experiments that cover a wide range of spatial and temporal scales. The model uses a standard upwind finite volume method and Roe's approximate Riemann solver for unstructured grids. A multidimensional linear reconstruction and slope limiter are implemented, achieving second-order spatial accuracy. Model efficiency and stability are treated using an explicit-implicit method for temporal discretization with operator splitting. Laboratory-and field-scale experiments were compiled where coupled processes across a range of scales were observed and where higher-order spatial and temporal accuracy might be needed for accurate and efficient solutions. These experiments demonstrate the ability of the fully coupled strategy in capturing dynamics of field-scale flood waves and small-scale drying-wetting processes.

Citation: Li, S., and C. J. Duffy (2011), Fully coupled approach to modeling shallow water flow, sediment transport, and bed evolution in rivers, *Water Resour. Res., 47*, W03508, doi:10.1029/2010WR009751.

1. Introduction

[2] Water flow and sediment transport are simultaneous and interactive processes in rivers, floodplains, and coastal areas. The interaction among these processes is influenced by both human activities and extreme natural events, resulting in aggradation and degradation in channels and harbors, deterioration of water quality and fisheries among other environmental effects, and many other forms of ecological disturbance. Examples include dam removal, dam break, and extreme storm events that induce rapidly varying flow and sediment flushing. The disturbance is complex because of the uneven and changing bottom topography, irregular boundaries, rapid and strong erosion with abrupt bed and flow variations, and complicated and uncertain flow-sediment transport mechanisms. Under these conditions, one-dimensional, uncoupled strategies are generally not sufficient, and two-dimensional approaches capable of handling complicated geometry, rapidly varying flow, and fully coupled physics are necessary. This research builds on recent advances for numerical solutions to fully coupled multiphysics problems in engineering and computational fluid dynamics to flow, sediment, and bed morphology interaction in rivers and tests the model over a range of scales in laboratory and field experiments.

[3] The shallow water equations are typically used to represent the hydrodynamics of river floods, storm surges, tidal fluctuations, tsunami waves, and forces acting on offshore structures [*Aizinger and Dawson*, 2002]. Methods for solving the shallow water equations include the method of characteristics [e.g., *Katopodes and Strelkoff*, 1978], finite difference [e.g., *Molls and Chaudhry*, 1995], finite element [e.g., *Hervouet*, 2000], and finite volume [e.g., *Alcrudo and Garcia-Navarro*, 1993; *Zhao et al.*, 1994; *Anastasiou and Chan*, 1997; *Sleigh et al.*, 1998; *Toro*, 2001; *Bradford and Sanders*, 2002; *Valiani et al.*, 2002; *Yoon and Kang*, 2004; *Begnudelli and Sanders*, 2006]. Although each method has its own strengths and limitations, it is generally true that unstructured grids have advantages for representing natural channels. An algorithm for "optimal" unstructured grids was proposed by *Shewchuk* [1997], which is able to provide an "optimal" representation of the domain with the least number of elements while still conforming to a limited set of physical and geometric constraints particular to the physical domain.

[4] With respect to the numerical method, the finite volume method allows for local and global mass conservation, can be applied to structured or unstructured grids, and requires less memory for explicit calculations as compared to finite difference or finite element methods [*Loukili and Soulaimani*, 2007]. Several investigators have solved the shallow water equations on unstructured grids using finite volume methods [*Zhao et al.*, 1994; *Anastasiou and Chan*, 1997; *Sleigh et al.*, 1998; *Yoon and Kang*, 2004], although sediment transport was not considered in those models. The coupled behavior of sediment transport and bed elevation

[1]Department of Civil and Environmental Engineering, Pennsylvania State University, University Park, Pennsylvania, USA.

0043-1397/11/2010WR009751

changes was experimentally studied by *Capart and Young* [1998], with implications for the dynamics of the flow regime as well. For coupled sediment transport and bed evolution the assumption of nonequilibrium conditions enforces a dynamic exchange between sediment deposition and entrainment, and this coupling is explored in this paper.

[5] Relatively few models and fewer field observations are available to study 2-D coupled hydrodynamic flow and sediment transport. An example is a large flood event or dam break on an initially dry surface where full water–sediment–bed form coupling is likely to be important. The dry-to-wet transition followed by a wet-to-dry transition with an evolving bed surface during postevent relaxation produces interesting multiscale behavior. Recently, several 1-D models were developed to simulate the dam-break-induced sediment transport or high-concentration sediment transport as in hyperconcentrated flow and debris flow [*Bellos and Hrissanthou*, 1998; *Fraccarollo et al.*, 2003; *Cao et al.*, 2004; *Ottevanger*, 2005; *Rosatti and Fraccarollo*, 2006; *Wu and Wang*, 2007]. *Hudson and Sweby* [2003] and *Castro Diaz et al.* [2008] discussed 1-D bed load transport models coupled with shallow water equations by finite volume methods. A few studies were found in the 2-D case. *Hudson and Sweby* [2005] and *Simpson and Castelltort* [2006] extended the 1-D models of *Hudson and Sweby* [2003] and *Cao et al.* [2004] to 2-D on structured grids, although the models were not tested in laboratory experiments or real flow fields in the field. *Liu et al.* [2008] developed a 2-D model of shallow water equations and bed load transport. Delft3D is capable of modeling 2-D and 3-D hydrodynamics and sediment transport using a finite difference method (http://delftsoftware.wldelft.nl/). Neither of these models considered the effects of suspended sediment on the hydrodynamics.

[6] In this paper we present a strategy for numerical solution of the system of fully coupled partial differential equations for 2-D shallow water flow, sediment transport, and bed evolution. We test the code against published laboratory, field, and numerical experiments to demonstrate the multiscale performance of the model. The model, referred to as PIHM_Hydro, is based on a cell-centered upwind finite volume method using Roe's approximate Riemann solver on an unstructured triangular grid. A multidimensional linear reconstruction technique and multidimensional slope limiter [*Jawahar and Kamath*, 2000] are implemented to achieve a second-order spatial accuracy. For model efficiency and stability, an explicit-implicit method is used in temporal discretization with operator splitting where advection and nonstiff source terms are solved via an explicit scheme with the stiff source terms handled by a fully implicit scheme. A number of test cases over a range of spatial scales and hydrological events are used to test the model and demonstrate the potential application. The code is open source and available from the authors.

2. Methodology

2.1. Mathematical Formulation

[7] Our system entails two-dimensional shallow water equations coupled with sediment mass conservation and bed topography evolution. The 2-D shallow water equations imply a negligible vertical velocity, hydrostatic pressure, and an incompressible fluid appropriate for vertically well-mixed water bodies. The system in conservative form is written as

$$\frac{\partial(\rho h)}{\partial t}+\frac{\partial(\rho uh)}{\partial x}+\frac{\partial(\rho vh)}{\partial y}=-\frac{\partial(\rho_z z)}{\partial t}+\rho_w S_p\,, \tag{1}$$

$$\frac{\partial(\rho uh)}{\partial t}+\frac{\partial\left[\rho\left(u^2h+\frac{gh^2}{2}\right)\right]}{\partial x}+\frac{\partial(\rho uvh)}{\partial y}=-\rho gh\left(S_{0x}+S_{fx}\right), \tag{2}$$

$$\frac{\partial(\rho vh)}{\partial t}+\frac{\partial(\rho uvh)}{\partial x}+\frac{\partial\left[\rho\left(v^2h+\frac{gh^2}{2}\right)\right]}{\partial y}=-\rho gh\left(S_{0y}+S_{fy}\right). \tag{3}$$

[8] Mass conservation equations are used to describe the sediment transport and morphological evolution process. There are two approaches to coupled sediment routing and bed evolution, i.e., noncapacity and capacity models (or, customarily, nonequilibrium and equilibrium). The noncapacity models represent the sediment in a single mode as the total load. Compared to capacity models, noncapacity models treat entrainment and deposition as independent processes, the difference between which influences the sediment discharge and morphological evolution. The noncapacity models facilitate the numerical formulation since the empirical entrainment and deposition functions can be treated as source terms. On the basis of this discussion, the noncapacity model is adopted here. The conservation of sediment suspended in the water column is given by

$$\frac{\partial(\psi h)}{\partial t}+\frac{\partial(\psi uh)}{\partial x}+\frac{\partial(\psi vh)}{\partial y}=E-D+S_s\,. \tag{4}$$

[9] A mass balance for local variation in the bed elevation as a function of sediment removed or accumulated is given by

$$(1-p)\frac{\partial z}{\partial t}=D-E\,, \tag{5}$$

where t is time, x and y are horizontal coordinates, h is flow depth, u and v are horizontal velocities, z is bed elevation, ψ is flux-averaged volumetric sediment concentration (L^3/L^3), g is gravitational acceleration (L/T^2), p is bed sediment porosity, ρ_z is density of saturated bed, ρ is density of the water-sediment mixture, S_{0x} and S_{0y} are the bed slopes in the x and y directions (L/L), S_{fx} and S_{fy} are x and y friction slopes (L/L), S_p are sources and sinks (e.g., precipitation, infiltration, etc.), S_s are sediment sources and sinks, and D and E are sediment deposition and entrainment fluxes across the river bed (L/T), respectively. The densities of the water-sediment mixture and saturated bed are given by

$$\rho=\rho_w(1-\psi)+\rho_s\psi\,, \tag{6}$$

$$\rho_z=\rho_w p+\rho_s(1-p)\,. \tag{7}$$

[10] We note in equation (4) that diffusive transport is treated as negligible [*Bennett*, 1974].

[11] Equation (1) differs from the traditional mass conservation equation for shallow water flow since the right-hand term accounts for the morphological change. We also note that variable fluid density in (1)–(3) allows fluvial processes to carry concentrated sediment flows.

[12] Following the approach by *Cao et al.* [2004], the system of equations (1)–(5) can be manipulated so that the mixture density appears on the right-hand side (i.e., in the source terms) to give

$$\frac{\partial h}{\partial t}+\frac{\partial (uh)}{\partial x}+\frac{\partial (vh)}{\partial y}=\frac{E-D}{1-p}+S_p+\frac{(\rho_w-\rho_s)S_s}{\rho_w}\,, \tag{8}$$

$$\begin{aligned}\frac{\partial (uh)}{\partial t}+\frac{\partial (u^2h+gh^2/2)}{\partial x}+\frac{\partial (uvh)}{\partial y}&=-gh\left(S_{0x}+S_{fx}\right)\\ &-\frac{(\rho_s-\rho_w)gh^2}{2\rho}\frac{\partial \psi}{\partial x}-\frac{(\rho_z-\rho)(E-D)u}{\rho(1-p)}\\ &+\left(\frac{\psi S_p}{\rho}-\frac{S_s}{\rho_w}\right)(\rho_s-\rho_w)u,\end{aligned} \tag{9}$$

$$\begin{aligned}\frac{\partial (vh)}{\partial t}+\frac{\partial (uvh)}{\partial x}+\frac{\partial (v^2h+gh^2/2)}{\partial y}&=-gh\left(S_{0y}+S_{fy}\right)\\ &-\frac{(\rho_s-\rho_w)gh^2}{2\rho}\frac{\partial \psi}{\partial y}-\frac{(\rho_z-\rho)(E-D)v}{\rho(1-p)}\\ &+\left(\frac{\psi S_p}{\rho}-\frac{S_s}{\rho_w}\right)(\rho_s-\rho_w)v.\end{aligned} \tag{10}$$

[13] In equations (9) and (10), there are two additional source terms. The second and third terms on the right-hand side account for the spatial variations in sediment column concentration and the momentum transfer, because of sediment exchange between the water and the erodible bottom boundary.

[14] Auxiliary equations for the bottom slope are given by $S_{0x}=\partial z/\partial x$ and $S_{0y}=\partial z/\partial y$, and the friction slope is estimated by the Manning equation:

$$S_{fx}=\frac{n^2u\sqrt{u^2+v^2}}{h^{4/3}}\,, \tag{11}$$

$$S_{fy}=\frac{n^2v\sqrt{u^2+v^2}}{h^{4/3}}\,, \tag{12}$$

where n is Manning's coefficient.

[15] For the sediment flux, there exists an extensive literature of empirical formulae [e.g., *Fagherazzi and Sun*, 2003; *Capart and Young*, 1998; *Cao et al.*, 2004; *Wu and Wang*, 2007]. A parsimonious form which captures the empirical physics for entrainment and deposition in a minimum of parameters is proposed by the authors based on those existing works:

$$E=\alpha(\theta-\theta_c)h\sqrt{u^2+v^2}\,, \tag{13}$$

$$D=\beta\omega\psi\,, \tag{14}$$

where α is a calibrated constant, $\theta=u_*^2/sgd$ is the Shields parameter, θ_c is the critical Shields parameter for initiation of sediment movement, β is a parameter which depends on the distribution of the sediment in water column, ω is the settling velocity of sediment particles in water, $u_*=\sqrt{gh}\sqrt{S_{fx}^2+S_{fy}^2}$ is the friction velocity, d is the sediment diameter, ν is the kinematic viscosity of water, and $s=\rho_s/\rho_w-1$. In this paper, following *Cao et al.* [2004], β is set as

$$\beta=\min[2,(1-p)/\psi]. \tag{15}$$

[16] And ω is calculated using

$$\omega=\sqrt{\left(13.95\frac{\nu}{d}\right)^2+1.09gsd}-13.95\frac{\nu}{d}\,. \tag{16}$$

2.2. Domain Decomposition

[17] Quality unstructured grids are generated by the well known Triangle algorithm of *Shewchuk* [2007]. Triangle allows the user to decompose the domain subject to constraints, such as boundaries, observation points, and/or nested multiresolution bathymetry [*Qu and Duffy*, 2007; *Kumar et al.*, 2008]. We have incorporated Triangle into an open source GIS (PIHM_GIS [*Bhatt et al.*, 2008]) to facilitate the generation of unstructured meshes using GIS feature objects.

2.3. Numerical Model

[18] The system of equations (8), (9), (10), (4) and (5) is hyperbolic and nonlinear and subject to discontinuities (shocks). Extending the 1-D formulation by *Fagherazzi and Sun* [2003], (5) is rewritten as

$$\frac{\partial \phi}{\partial t}+\frac{\partial (\psi uh)}{\partial x}+\frac{\partial (\psi vh)}{\partial y}=S_s\,, \tag{17}$$

with

$$\phi=(1-p)z+\psi h\,. \tag{18}$$

[19] The system is now conveniently expressed in vector form:

$$\frac{\partial \mathbf{U}}{\partial t}+\frac{\partial \mathbf{E}}{\partial x}+\frac{\partial \mathbf{G}}{\partial y}=\mathbf{S}\,, \tag{19}$$

where $\mathbf{U}$ is a vector of the conservative variables, $\mathbf{E}$ and $\mathbf{G}$ are the flux vectors in the x and y directions, and $\mathbf{S}$ is the vector of source terms.

$$\mathbf{U}=\begin{pmatrix}h\\ uh\\ vh\\ \psi h\\ \phi\end{pmatrix},\ \mathbf{E}=\begin{pmatrix}uh\\ u^2h+\frac{gh^2}{2}\\ uvh\\ \psi uh\\ \psi uh\end{pmatrix},\ \mathbf{G}=\begin{pmatrix}vh\\ uv\\ v^2h+\frac{gh^2}{2}\\ \psi vh\\ \psi vh\end{pmatrix},\quad \mathbf{S}=\begin{pmatrix}\frac{(E-D)}{1-p}+S_p+\frac{(\rho_w-\rho_s)S_s}{\rho_w}\\ S_x\\ S_y\\ E-D+S_s\\ S_s\end{pmatrix}. \tag{20}$$

with

$$\begin{aligned}S_x=-gh\left(S_{0x}+S_{fx}\right)&-\frac{(\rho_s-\rho_w)gh^2}{2\rho}\frac{\partial \psi}{\partial x}-\frac{(\rho_z-\rho)(E-D)u}{\rho(1-p)}\\ &+\left(\frac{\psi S_p}{\rho}-\frac{S_s}{\rho_w}\right)(\rho_s-\rho_w)u\,,\end{aligned} \tag{21}$$

$$S_y = -gh(S_{0y} + S_{fy}) - \frac{(\rho_s - \rho_w)gh^2}{2\rho}\frac{\partial \psi}{\partial y} - \frac{(\rho_z - \rho)(E-D)v}{\rho(1-p)} + \left(\frac{\psi S_p}{\rho} - \frac{S_s}{\rho_w}\right)(\rho_s - \rho_w)v\,. \tag{22}$$

[20] The source term vector now has five parts: bed slope $\mathbf{S_0}$, friction slope $\mathbf{S_f}$, sediment concentration variations $\mathbf{S_c}$, sediment exchange $\mathbf{S_e}$, and the additional source-sink term $\mathbf{S_p}$:

$$\mathbf{S_0} = (\,0 \quad -ghS_{0x} \quad -ghS_{0y} \quad 0 \quad 0\,)^T, \tag{23}$$

$$\mathbf{S_f} = (\,0 \quad -ghS_{fx} \quad -ghS_{fy} \quad 0 \quad 0\,)^T, \tag{24}$$

$$\mathbf{S_c} = \left(0 \quad -\frac{(\rho_s-\rho_w)gh^2}{2\rho}\frac{\partial \psi}{\partial x} \quad -\frac{(\rho_s-\rho_w)gh^2}{2\rho}\frac{\partial \psi}{\partial y} \quad 0 \quad 0\right)^T, \tag{25}$$

$$\mathbf{S_e} = \left(\frac{E-D}{1-p} \quad -\frac{(\rho_z-\rho)(E-D)u}{\rho(1-p)} \quad -\frac{(\rho_z-\rho)(E-D)v}{\rho(1-p)} \quad E-D \quad 0\right)^T, \tag{26}$$

$$\mathbf{S_p} = \left(S_p + \frac{(\rho_w - \rho_s)S_s}{\rho_w}\left(\frac{\psi S_p}{\rho} - \frac{S_s}{\rho_w}\right)(\rho_s - \rho_w)u \times \left(\frac{\psi S_p}{\rho} - \frac{S_s}{\rho_w}\right)(\rho_s - \rho_w)v \; S_s \; S_s\right)^T. \tag{27}$$

[21] It is now convenient to write the system as

$$\frac{\partial \mathbf{U}}{\partial t} + \nabla \times \mathbf{F} = \mathbf{S}\,, \tag{28}$$

where $\mathbf{F} = (\mathbf{E}, \mathbf{G})^T$. The system is then integrated over an arbitrary control volume V_i (a triangular element here):

$$\int_{V_i} \frac{\partial \mathbf{U}}{\partial t} dV + \int_{V_i} \nabla \times \mathbf{F} dV = \int_{V_i} \mathbf{S} dV\,. \tag{29}$$

[22] Application of the Gauss theorem leads to the integral form of (29):

$$\int_{V_i} \frac{\partial \mathbf{U}}{\partial t} dV + \oint_{\Gamma_i} \mathbf{F} \times \mathbf{n} d\Gamma = \int_{V_i} \mathbf{S} dV\,, \tag{30}$$

where Γ is the boundary of the control volume and $\mathbf{n} = (n_x \; n_y)^T$ is the unit outward vector normal to the boundary.

[23] A cell-centered finite volume is used to approximate (30) by vertically projecting a Delaunay triangle to form the prismatic control volume (Figure 1). The state variables of the system are stored at the centroid of the control volume and represented as piecewise constant over the domain. We note that by solving the system for the centroid of each finite volume enables the implementation of a high-order interpolation scheme [*Sleigh et al.*, 1998], discussed in section 2.4. Finally, (30) is rewritten as

$$\frac{\partial \mathbf{U}_i}{\partial t} = -\frac{1}{V_i}\sum_{j=1}^{3} (\mathbf{F}_{ij} \times \mathbf{n}_{ij})\Gamma_j + \mathbf{S}_i\,, \tag{31}$$

where $\mathbf{U}_i$ again refers to average values over the control volume V_i, $\mathbf{S}_i = 1/V_i \int_{V_i} \mathbf{S} dV$ is the numerical approximation of the source term, $\mathbf{n}_{ij}$ is the unit outward normal vector to the edge j, Γ_j is then length of edge j, and $\mathbf{F}_{ij}$ is the numerical flux vector through the edge j, which is calculated using an approximate Riemann solver [*LeVeque*, 2002]. Details of the flux evaluation using an approximate Riemann solver are found in Appendix A, including a discussion of the strategy for handling discontinuities and Roe's formulation and the numerical flux evaluation at element boundaries [*Sleigh et al.*, 1998].

2.4. Linear Reconstruction and Multidimensional Slope Limiter

[24] In PIHM_Hydro we attempt to preserve high spatial accuracy in the flow simulation by adopting a second-order piecewise linear reconstruction. Many second-order numerical schemes have been implemented for shallow water equations on unstructured triangular grids [e.g., *Anastasiou and Chan*, 1997; *Sleigh et al.*, 1998; *Hubbard*, 1999; *Wang and Liu*, 2000; *Yoon and Kang*, 2004] and other types of grids as well [e.g., *Alcrudo and Garcia-Navarro*, 1993; *Ambrosi*, 1995; *Valiani et al.*, 2002; *Caleffi et al.*, 2003]. Extension of structured techniques to unstructured grids such as the MUSCL approach have achieved only partial success because of the pronounced grid sensitivity [*Jawahar and Kamath*, 2000], with poor results typically obtained on highly distorted grids. The reconstruction technique proposed by *Jawahar and Kamath* [2000] was successfully applied with the Harten–Lax–van Leer (HLL) approximate Riemann solver for shallow water equations [*Yoon and Kang*, 2004]. Compared to other multidimensional linear reconstruction techniques, this one uses a wide computational stencil and does not strongly depend on vertex values. It has also been shown that high-order schemes may lead to nonphysical oscillatory solutions near discontinuities [*Toro*, 1999]. To avoid oscillations, we limit the solution slope during the linear reconstruction. The multidimensional slope limiter proposed by *Jawahar and Kamath* [2000] has the advantages that (1) the limiter is inherently multidimensional which fits unstructured grids and (2) it is continuously differentiable.

2.5. Source Terms

[25] It was found that the source terms in (23)–(27) require careful treatment. The friction slope $\mathbf{S_f}$ and sediment exchange $\mathbf{S_e}$ were discretized in a pointwise manner and evaluated at the element centroid. The sediment concentration $\mathbf{S_c}$ terms are also discretized at the centroid, and the linear reconstruction procedure readily provides the gradient of sediment concentration (ψ):

$$\nabla \psi_i = \frac{\nabla (h\psi)_i - \psi \nabla h_i}{h}\,. \tag{32}$$

2.6. Time Integration

[26] A critical problem in our coupled system is the numerical instabilities related to friction slope and sediment exchange for shallow depths. A semi-implicit method is used, where the system (31) is split into two systems of ordinary differential equations:

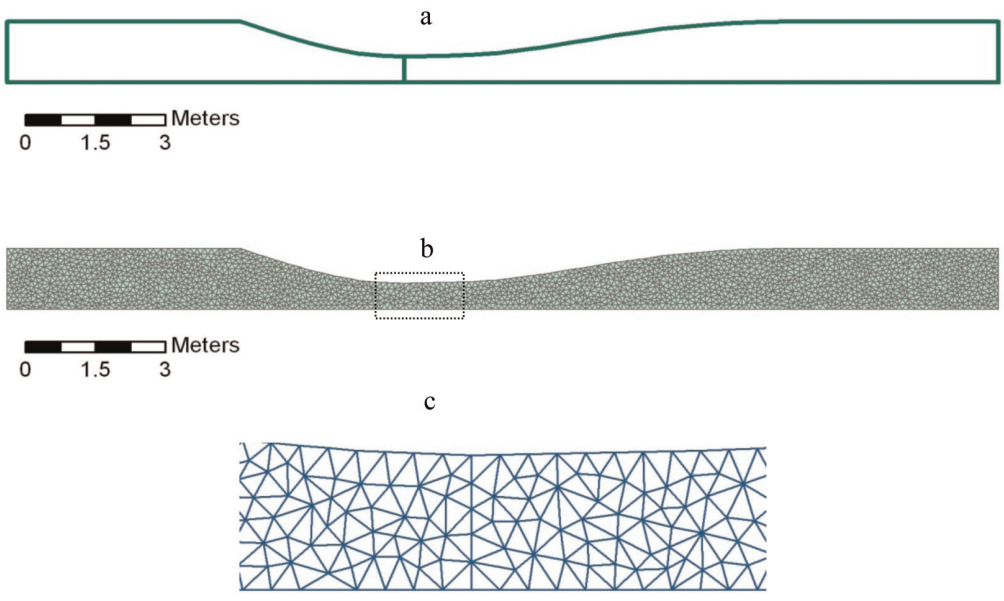

Figure 1. (a) Plan view, (b) computational mesh, and (c) close-up view of the near-dam area of the converging-diverging channel in *Bellos et al.*'s [1992] experiment.

$$\frac{\partial \mathbf{U}_i}{\partial t} = -\frac{1}{V_i}\sum_{j=1}^{3}\left(\mathbf{F}_{ij}\times\mathbf{n}_{ij}\right)\Gamma_j + \mathbf{S}_{\mathbf{0}i} + \mathbf{S}_{\mathbf{c}i} + \mathbf{S}_{pi}\,, \tag{33}$$

$$\frac{\partial \mathbf{U}_i}{\partial t} = \mathbf{S}_{\mathbf{f}i} + \mathbf{S}_{\mathbf{e}i}\,. \tag{34}$$

[27] In the first step, advection and source terms for bed slope and sediment concentration are solved using an explicit method. Then, the values obtained from the first step define initial conditions for the remaining equations, which use an implicit method (backward differentiation formula). PIHM_Hydro uses the advanced ODE solver CVODE [*Hindmarsh and Serban*, 2005].

[28] Explicit time integration is performed by the first-order Euler method or a total variation diminishing Runge-Kutta method [*Shu and Osher*, 1988] given by

$$\begin{aligned}\mathbf{U}_1 &= \mathbf{U}^n + \Delta t f(\mathbf{U}^n),\\ \mathbf{U}_2 &= \frac{3}{4}\mathbf{U}^n + \frac{1}{4}\mathbf{U}_1 + \frac{1}{4}\Delta t f(\mathbf{U}_1),\\ \mathbf{U}^{n+1} &= \frac{1}{3}\mathbf{U}^n + \frac{1}{3}\mathbf{U}_2 + \frac{2}{3}\Delta t f(\mathbf{U}_2),\end{aligned} \tag{35}$$

where f is the right-hand side of (33). The method has been shown to improve stability and preserves high-order accuracy (third) [*Shu and Osher*, 1988].

[29] It is well known that the explicit scheme has a stability restriction on the Courant-Friedrichs-Lewy condition. An adaptive Δt is used in the model using the following:

$$\Delta t \le \frac{\min(d_i)}{2\max\left[\left(\sqrt{u^2+v^2}+c\right)_i\right]}\,, \tag{36}$$

where i is the cell index and d_i represents the whole set of distances between the ith centroid and those of its neighboring cells.

2.7. Boundary Conditions

[30] Open and solid wall boundary conditions have been implemented. The left-hand (slip) solid wall boundary condition is given by

$$\begin{pmatrix} h_* \\ \mathbf{u}_*\times\mathbf{n} \\ \mathbf{u}_*\times\mathbf{t} \\ \psi_* \\ z_* \end{pmatrix} = \begin{pmatrix} h_L \\ -\mathbf{u}_\mathbf{L}\times\mathbf{n} \\ \mathbf{u}_\mathbf{L}\times\mathbf{t} \\ \psi_L \\ z_L \end{pmatrix}, \tag{37}$$

where $\mathbf{u}$ denotes $(u, v)^T$ and the subscripts L and asterisk are the variables at the left side and boundary, respectively. The velocity components can be calculated by

$$\begin{pmatrix} u_* \\ v_* \end{pmatrix} = \begin{pmatrix} n_x & -n_y \\ n_y & n_x \end{pmatrix}\begin{pmatrix} \mathbf{u}_L\times\mathbf{n} \\ \mathbf{u}_L\times\mathbf{t} \end{pmatrix}. \tag{38}$$

[31] The open boundary conditions are more complicated. A simple one is the free outfall condition, where the waves pass the boundary without reflection. It can be described as $\mathbf{U}_* = \mathbf{U}_L$. For other cases, it is sometimes found that the physical boundary condition(s) is not sufficient, and the theory of characteristics is used to derive sufficient information at the boundaries. For more detailed discussion about the open boundary conditions, refer to *Zhao et al.* [1994], *Anastasiou and Chan* [1997], and *Sleigh et al.* [1998].

[32] A very small flow depth commonly occurs near the wetting-drying boundaries, which introduces numerical instabilities with unreliably high velocities that make the friction slope and sediment source terms (equations (24) and (26)) very stiff, as mentioned. To solve this problem, in addition to employing the semiexplicit time integration scheme, a simple wetting-drying algorithm was also implemented. In this approach, a tolerance depth (h_{tol}) was chosen in that the flow velocities were set to zero when the

flow depth was less than h_{tol}. In each example h_{tol} was chosen empirically.

3. Field and Laboratory Implementation

[33] The first objective of this research was to develop a robust fully coupled numerical code suitable for applications over a wide range of spatial and temporal scales and riverine processes for flow, sediment, and bed evolution. A second objective was to bring together experimental data sets to test and compare PIHM_HYDRO over a useful range of spatial and temporal scales and also to compare the model with other published models. For the laboratory scale, we found three examples that represent small-scale hydrodynamics and sediment transport, and two examples were developed for the field-scale application. Each of the four experimental results is available at http://www.pihm.psu.edu for the purpose of future experimental and model testing.

3.1. Two-Dimensional Laboratory-Scale Dam Break With a Dry-Wet Transition and Converging-Diverging Channel

[34] *Bellos et al.* [1992] performed simulations of instantaneous dam failure for a range of initial conditions. This experiment is used to test PIHM_Hydro for simulating flow dynamics in an irregular flow domain with an initially dry bed with nonzero bed slope and roughness. The 21.2 m × 1.4 m wide experimental flume had a rectangular, converging-diverging cross section (Figure 4). A movable gate ($x = 0$ m) was used to simulate the instantaneous dam break. Eight probes were installed along the centerline of the channel to measure the flow depths.

[35] The initial water level is 0.15 m upstream of the dam and zero downstream from the dam with the bed slope of 0.002. A solid wall boundary condition was applied at the upstream end and sidewalls, and a free out-fall condition was applied at the downstream boundary. The domain was discretized into 3886 triangles (Figure 1). The Nash-Sutcliffe model efficiency coefficient (NSE) [*Nash and Sutcliffe*, 1970] was used to quantitatively evaluate the accuracy of the model for observed and predicted quantities. The predicted and measured flow depths at the different positions are shown in Figure 2.

[36] Upstream of the dam the predictions match the measurements very well with minimal error. At downstream locations where critical to supercritical flow and the wetting-drying process is observed, the flow depths are still well reproduced. However, it was found that downstream locations ($x = +5.0$ m) were quite sensitive to Manning's roughness coefficient, possibly because of depth averaging and lack of a vertical velocity term in the transition from subcritical to supercritical flow [*Martin and Gorelick*, 2005]. Figure 2 reveals that the arrival times of the wavefront are accurately simulated, and for this small-scale test case the model was found to be both accurate and stable for the wetting-drying process as well as for supercritical flows. The model is able to simulate the early time and late time behavior of the flood waves as well as the sharp propagation of the drying front. Sediment transport was not considered in the original experiment, and other model simulations were not found for this experiment.

3.2. Case 2: Two-Dimensional Rainfall-Runoff Numerical Experiment With Wetting-Drying Surface

[37] A rainfall-runoff numerical experiment by *diGiammarco et al.* [1996] was used to compare simulations of rainfall-driven flow with rapid wetting-drying of the surface. In this example, a tilted V-shaped catchment (Figure 3) is generated by introducing a single, 90 min duration, 10.8 mm/h intensity rainfall event. The catchment is composed of two 1000 m × 800 m planes connected by a 1000 m long × 20 m wide channel. Infiltration is zero over the entire domain. In this case the channel depth is set to zero which means the planes and channel are continuously connected so that a backwater effect could be considered. The bed slopes are 0.05 and 0.02, perpendicular to and parallel to the channel, respectively. Manning roughness coefficients are 0.015 s/m$^{1/3}$ for the plane and 0.15 s/m$^{1/3}$ for the channel. The simulation was run for 180 min with a free boundary condition at the channel outlet and no-flow boundary conditions elsewhere. Initially, the water depth is zero over the entire domain.

[38] The simulation used 740 triangles and was compared with integrated finite difference (IFD) [*diGiammarco et al.*, 1996], MIKE-SHE [*Abbot et al.*, 1986], IHM [*VanderKwaak*, 1999], and MODHMS [*Panday and Huyakorn*, 2004], all of which use either the kinematic or diffusive approximations. In these models, IFD, MIKE-SHE, and MODHMS weakly couple the 2-D flow on the plane with the 1-D flow in the channel, while IHM fully couples the 2-D flows on the plane and in the channel. The hydrograph predicted by PIHM_Hydro is compared with the multimodel average in Figure 4a. The multimodel average is the mean value of all model outputs. PIHM_Hydro is also compared individually with IFD, MIKE-SHE, IHM, and MODHMS in Figure 4a. The simulation data from these models were obtained by digitizing the figures from the publications, which introduced some error.

[39] Excellent agreement is illustrated between PIHM_Hydro and the multimodel average (using Nash-Sutcliff criteria) as with the other models, especially for the peak discharge and receding limb. Although there is a slight discrepancy in the rising limb for these models, the times to peak discharge are almost identical. According to Figure 4a, PIHM_Hydro predicts a constant and stable plateau of the peak discharge (4.86 m^3/s), which is analytically correct and shows the model to be stable. Among these simulations, PIHM_Hydro had the closest agreement with IHM, followed by MODHMS, MIKE-SHE, and IFD. respectively, again using Nash-Sutcliff criteria. One possibility for the similarity is that only PIHM_Hydro and IHM fully couple the 2-D overland and channel flow to consider the backwater effect. Figure 4b shows the accumulative mass balance errors calculated using the equation

$$\mathrm{err}_h = \frac{(\text{precipitation} - \text{discharge} - \text{storage})}{\text{precipitation}}. \qquad (39)$$

[40] The mass balance error is very small, with the maximum value less than 0.8% at $t = 45$ min and almost zero at $t = 180$ min. For this benchmark case, PIHM-Hydro performance is stable and mass conservative for cases of rainfall-driven overland channel flow and intensive wetting-drying processes.

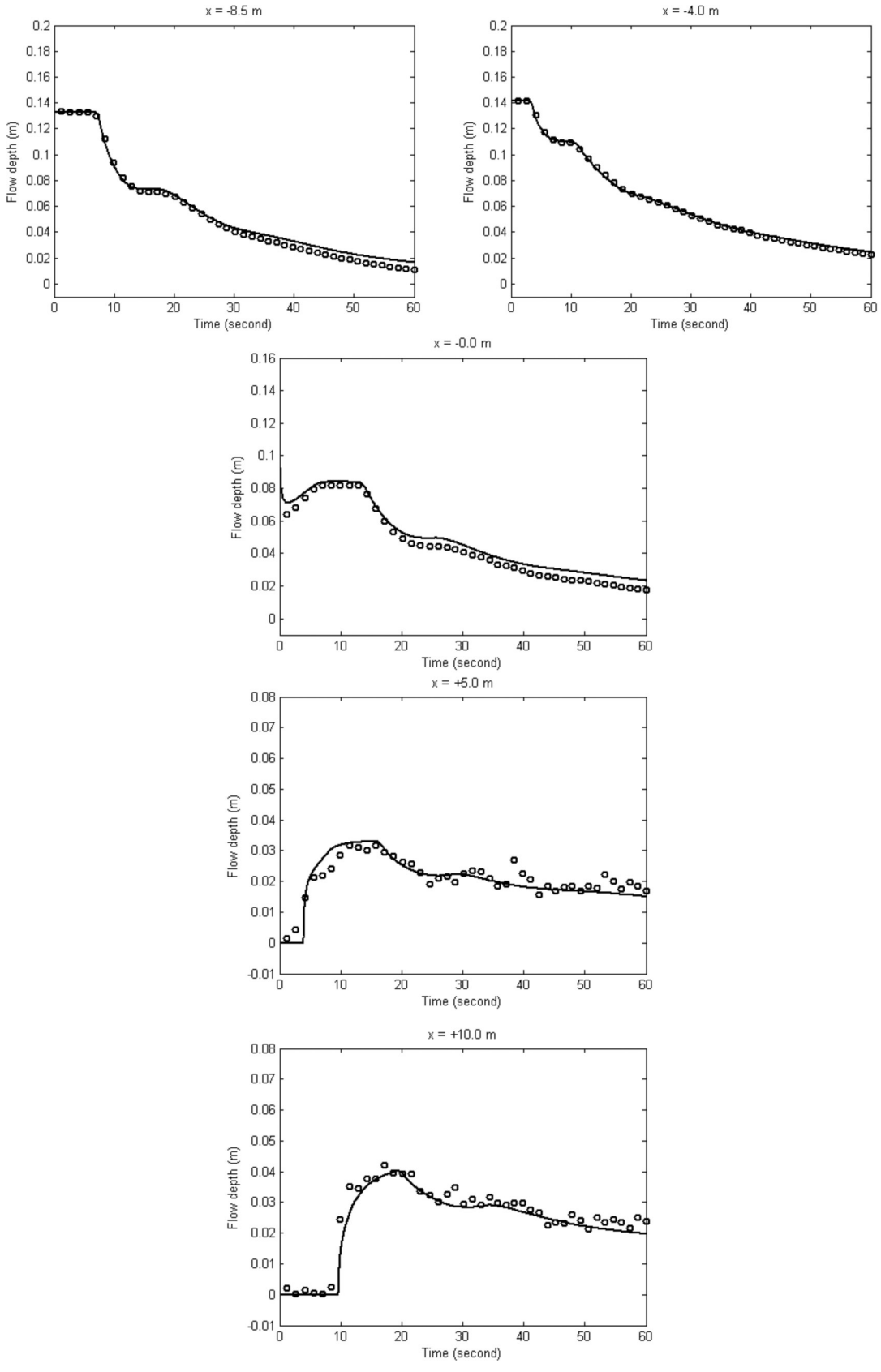

Figure 2. Two-dimensional laboratory-scale dam break with dry-wet and converging-diverging channel: measured (circles) and predicted (solid line) temporal variations of flow depth at different locations upstream of the dam, at the dam, and downstream from the dam. Not all locations shown have observed data.

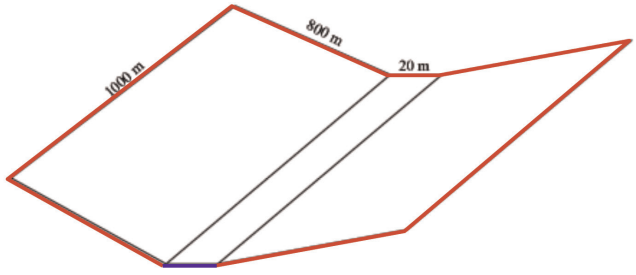

Figure 3. Two-dimensional rainfall-runoff dry to wet numerical experiment: tilted V-shaped catchment (not to scale). The red lines represent the no-flow boundaries. The blue line denotes the channel outlet, where the free outfall boundary is applied [*diGiammarco et al.*, 1996]. The black lines are the break in slope between side slope planes and the channel. The side slope is 0.05, and the bed slope is 0.02.

3.3. Case 3: Two-Dimensional Laboratory-Scale Flow and Sediment Transport Following Dam Break

[41] In this test case, model flow dynamics with fully coupled sediment transport is implemented for two laboratory-scale dam break experiments with flow over movable beds. These are described in the literature as the Taipei experiment [*Capart and Young*, 1998] and the Louvain experiment [*Fraccarollo and Capart*, 2002]. In the Taipei experiment, sediment particles were artificial spherical beads of uniform size diameter of 6.1 mm, specific gravity of 1.048, and settling velocity of 7.6 cm/s. In the Louvain experiment, the sediment particles were replaced by cylindrical PVC pellets with equivalent spherical diameter of 3.5 mm, specific gravity of 1.54, and settling velocity of 18 cm/s. Horizontal prismatic flumes were used in both experiments. The test reach was 1.2 m long, 70 cm high, and 20 cm wide for the Taipei experiment and 2.5 m long, 25 cm high, and 10 cm wide for the Louvain experiment. The sluice gates were placed in the middle of the flumes in both cases to represent the dam break. The initial water depth was 10 cm upstream and 0 cm downstream for both experiments. The solid wall boundary condition was applied to all the boundaries.

[42] The 2-D computational meshes are shown in Figure 5, with 745 and 764 triangles for the Taipei and Louvain experiments, respectively. In this model, several parameters need to be determined. The sediment porosity (p) and Manning's roughness coefficient (n) were obtained from the literature [*Wu and Wang*, 2007]. Here p was set to 0.28 and 0.3 for the Taipei and Louvain experiments, respectively, while n was set as 0.025 s/m$^{1/3}$ for both experiments. For the parameters α and θ_c, calibration was done using measured data at $5t_0$ and $3t_0$ ($t_0 = 0.101$ s) for the Taipei and Louvain experiments, respectively, and the calibrated parameters were then used to predict the flow and sediment dynamics for the other two times. Parameters α and θ_c were calibrated to 2.2 and 0.15 for the Taipei example and 5.0 and 0.05 for the Louvain case.

[43] In Figures 6 and 7, the predicted water (H) and bed (z) surface elevations along the centerline of the channel are compared with the measured values. Nash-Sutcliff criteria were used to compare modeled and observed surface elevations for the two experiments. In the Louvain experiment, the measured data at $5t_0$ were used to calibrate the model for the same unknown parameters as before. In general, the model reproduced the flow dynamics over movable beds very well. Although the prediction of bed surface elevations is not as good as the water surface, it can be considered satisfactory considering the complexity of the bed evolution, the small timescale, the small magnitude of the bed elevation change, and the measurement uncertainty. According to Figure 6, the model predictions of the wavefront locations and the erosion magnitude were in fairly good agreement with the measurement in the experiment. A hydraulic jump formed near the initial dam sites because of rapid bed erosion. In the Louvain experiment, the location of the hydraulic jump was well predicted by the model. It can be observed from both the predictions and measurements that the hydraulic jump propagated upstream in the Louvain experiment.

[44] In the Taipei experiment, the measured data at $3t_0$ were used to calibrate the model. It is evident that the calibration is not as good as that in the Louvain experiment. By using the calibrated parameters, Figure 7 shows that the model predicted the wavefront location and the erosion magnitude quite well. However, the agreement between the prediction and measurement was not as good for the magnitude and the locations of the hydraulic jump (Figure 10). The hydraulic jump moved upstream in the prediction but remained stationary in the experiment. The cause needs further investigation.

[45] The mass balance errors of sediment transport were calculated using

$$\mathrm{err}_z = \frac{\sum_i (\Delta z)_i \times A_i (1-p) + \sum_i \Delta(hc)_i \times A_i^{t=5t_0}}{\sum_i (\Delta z)_i \times A_i}, \qquad (40)$$

where $(\Delta z)_i$ and $\Delta(hc)_i$ are the change of bed elevation and sediment load per area at each grid i. In the Louvain experiment, the err_z values are 0.05%, 0.007%, and 0.05% at $5t_0$, $7t_0$, and $10t_0$, respectively. In the Taipei experiment, the err_z values are 0.02%, 0.005%, and 0.001% at $3t_0$, $4t_0$, and $5t_0$, respectively. Mass balance errors are very small in each case.

[46] Figure 8 shows the predicted sediment concentration profiles in both experiments at different times. The model predicts sharp forefronts of the sediment concentration profile, which were caused by extremely high sediment

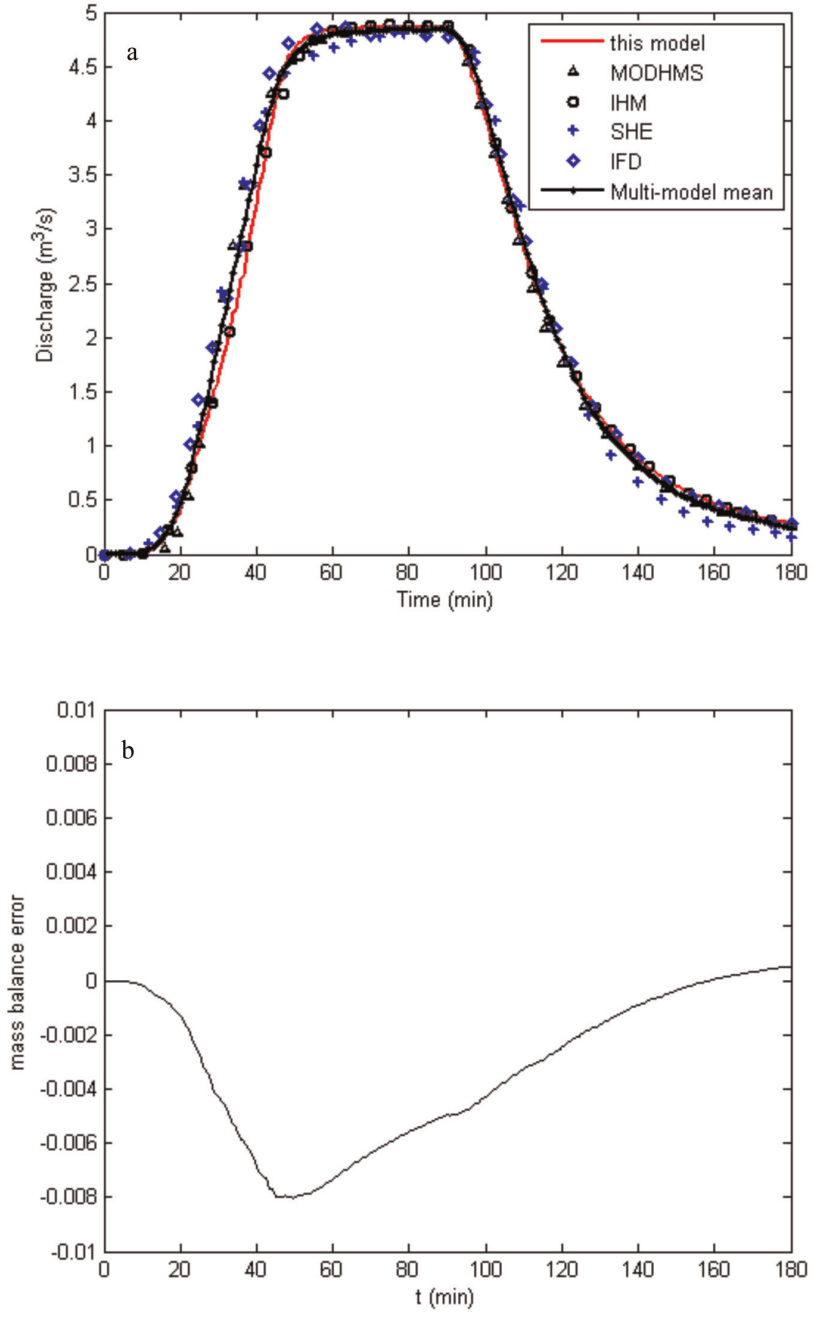

Figure 4. Evaluation of model performance for the 2-D rainfall-runoff dry to wet numerical experiment. (a) Comparison of simulated hydrograph with MODHMS [*Panday and Huyakorn*, 2004], IHM [*VanderKwaak*, 1999], MIKE-SHE [*Abbot et al.*, 1986], and IFD [*diGiammarco et al.*, 1996] and (b) mass balance errors.

concentrations in the dam break wavefronts. Similar predictions were also made by several 1-D models [*Fraccarollo and Capart*, 2002; *Wu and Wang*, 2007] in the Taipei case at $4t_0$. In the Wu and Wang model, however, a small initial downstream flow depth was specified rather than the actual dry bed condition, which may have caused errors in mass balance and wave arrival time. By comparing Figures 8a and 8b, it is noted that the peak concentrations in the Taipei case were much higher than those in the Louvain case. The difference is because of the smaller density and lower settling velocity of sediment particles in the Taipei case which make erosion easier and deposition slower. It is also noted that the peak sediment concentration decreased with time in the Louvain case while it increased with time in the Taipei case during their time scales. This difference is partly related to the different time scales of the two cases, where the Taipei experiment is run for a shorter duration than the Louvain experiment.

[47] Figure 9 illustrates the temporal variations of flow depths, flow discharge, and sediment discharge predicted

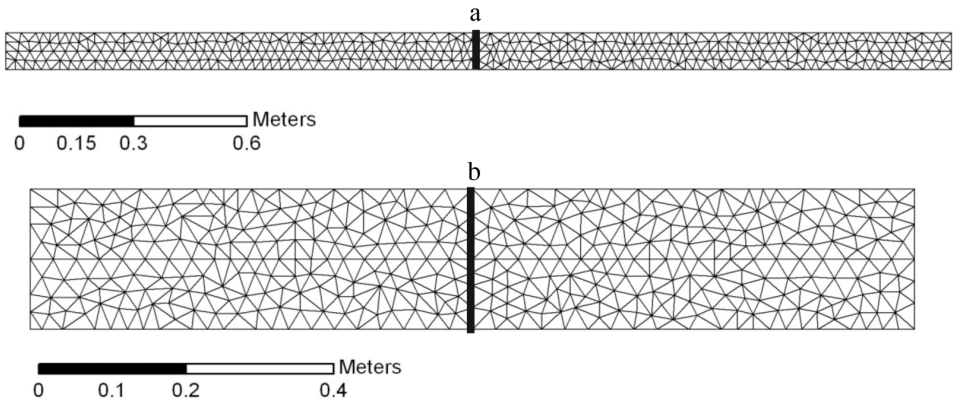

Figure 5. Plan view of the computational mesh for (a) the Louvain experiment and (b) the Taipei experiment. The thick vertical lines denote the dam in each case.

by this model at $x = 0.03$, 0.2, and 0.4 m. We observed that the flow depth and flow and sediment discharges approach equilibrium values after a period of time. In Figures 8 and 9 it is also found that volumetric sediment concentration, flow depth, and sediment discharge were very sensitive to particle size and density while discharge was not. Likewise, sediment discharge is also affected by the sediment particle properties indirectly. Overall erosion and deposition alter the bed surface, which in turn influences the flow depth profile.

3.4. Case 4: River and Floodplain Dynamics During Malpasset Dam Break Event

[48] Case 4 involves an actual dam break and flood wave propagating over a dry bed with complex topography and boundaries. The Malpasset dam was located in a narrow gorge of the Reyran river valley, about 12 km upstream of Frejus in southern France. The maximum reservoir capacity was 55,106 m^3. In December 1959, the dam failed explosively at night, partly because of exceptionally heavy rain. The flood wave propagated along the Reyran valley to the city of Frejus, and 433 casualties were reported. Details of this catastrophe are given by *Soares Frazão et al.* [1999].

[49] The topography of the computation domain is shown in Figure 10 with the location of dams, transformers, gauges, and police survey points [*Soares Frazão et al.*, 1999], with the solution domain encroaching on the shallow tidal estuary. The bottom elevation ranges from −20 m below sea level to 100 m above sea level. The domain was discretized into different resolution meshes using the domain boundary and the 13,541 topography survey points as the constraints. The 38,208-triangle mesh and a close-up view of the computational mesh near the dam are presented in Figure 11. The mesh is much finer immediately downstream from the dam and along the river, where rapid and abrupt flow occurred. The initial water level in the reservoir is 100 m above sea level and the channel bottom downstream from the dam is set dry in the model. The solid wall condition is imposed along all boundaries. The Strickler coefficient ranges from 30 to 40 $m^{1/3}/s^1$ [e.g., *Soares Frazão et al.*, 1999; *Hervouet and Petitjean*, 1999], corresponding to Manning's coefficient from 0.033 to 0.025 $s/m^{1/3}$. A uniform Manning coefficient of 0.033 $s/m^{1/3}$ was advised by other researchers [e.g., *Goutal*, 1999; *Hervouet*, 2000; *Valiani et al.*, 2002]. The sensitivity of the model to the Manning's coefficient was first studied on a 26,000-element triangle mesh (Table 1). It shows that PIHM_Hydro does work best at $n = 0.033$ $s/m^{1/3}$, which is in agreement with the previous studies as well as the recommendation for winding natural rivers by *Henderson* [1966].

[50] Table 2 shows how the grid resolution or terrain resolution influences the numerical solutions. Because of the large magnitude of water surface elevations, both NSE and root-mean-square error (RMSE) are used here to quantitatively assess the prediction errors. It is evident that the finer spatial resolutions produce better solutions, up to the point when the grid resolution reaches ∼38,208 in this case, and accuracy does not improve much even if the grids get much finer. By comparing the two metrics at the gauge stations and the police survey points in Table 2, we can see that the maximum water surface elevations (H) at the gauge points are more sensitive to the grid and terrain resolutions than those at the police survey points. This is because the magnitudes of the water depths (h) in the river are larger than the bed elevation (z), while along the banks the bed elevations are larger. The maximum water surface elevation is a reasonable metric to assess the model accuracy. Tables 1 and 2 illustrate that when the number of grids reaches 26,000, the simulation becomes satisfactory for all measurement locations according to our NSE criterion and that increasing the resolution to 38,208 grids provides some improvement, while finer-resolution grids do not significantly improve results.

[51] To examine the convergence of the model with successive grid refinement, we evaluated Roache's grid convergence index [*Roache*, 1994] at each gauge point. From this analysis a 38,208-grid mesh with $n = 0.033$ $s/m^{1/3}$ was found to provide the best result and was used to compare PIHM_Hydro with other models of the Malpasset dam break.

[52] The predicted evolution of flood inundation is shown with the police-surveyed points in Figure 12. The cells with a water depth smaller than 0.01 m are considered

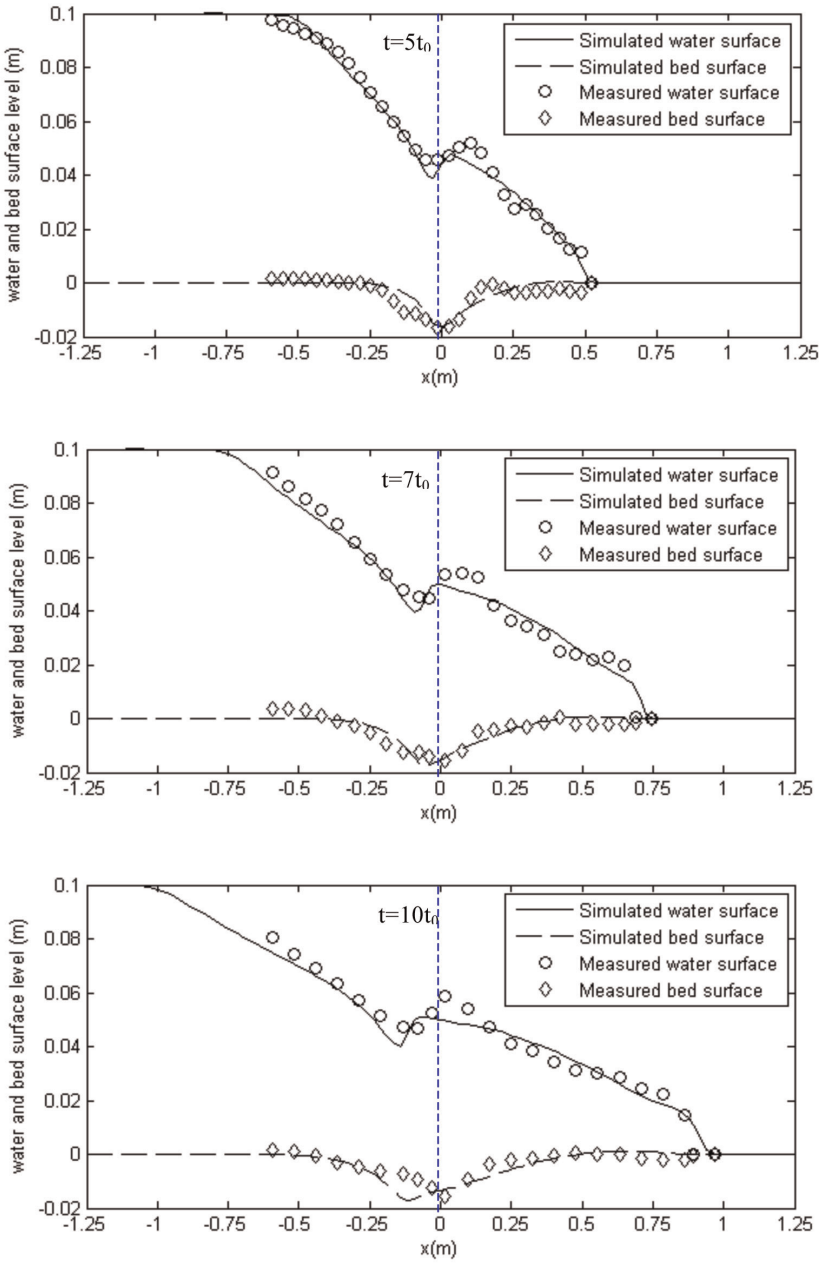

Figure 6. Water and bed surface levels along the centerline in the Louvain experiment ($t_0 = 0.101$ s). The vertical dashed line is the dam location.

dry. The police-surveyed points are high-water marks, which are considered to represent the flooded boundary. As can be seen from Figure 12, the model-predicted flood area agrees with the police survey quite well. Table 3 compares the computed arrival times of the flood waves at three electric transformers with simulations from *Hervouet and Petitjean* [1999], *Valiani et al.* [2002], and *Yoon and Kang* [2004]. Hervouet and Petitjean's model is based on a finite element method (FE) using unstructured triangular grids, while Valiani et al. and Yoon and Kang's models were developed by the HLL finite volume method (FV) on unstructured triangular and quadrilateral grids, respectively. The exact arrival times of the flood wavefront are unknown, and the measurements were affected by some uncertainties, e.g., the precise rupture time of the dam. Therefore, in addition to the arrival time, the travel time of the flood wave between two points is also an important criterion for judging the performance of a model.

[53] Note, in Table 3 that the arrival times and travel times of the flood waves predicted by PIHM_Hydro are in excellent agreement with the measurement with the maximum error ~2%. More importantly, PIHM_Hydro performs better than the other schemes for predicting the arrival time when the flood has traveled a large distance downstream. Although there are uncertainties in the data, from Table 3, we can see that PIHM_Hydro has only a 2% error in the arrival time at site C, while the other models vary from 12% to nearly 50% error in arrival time.

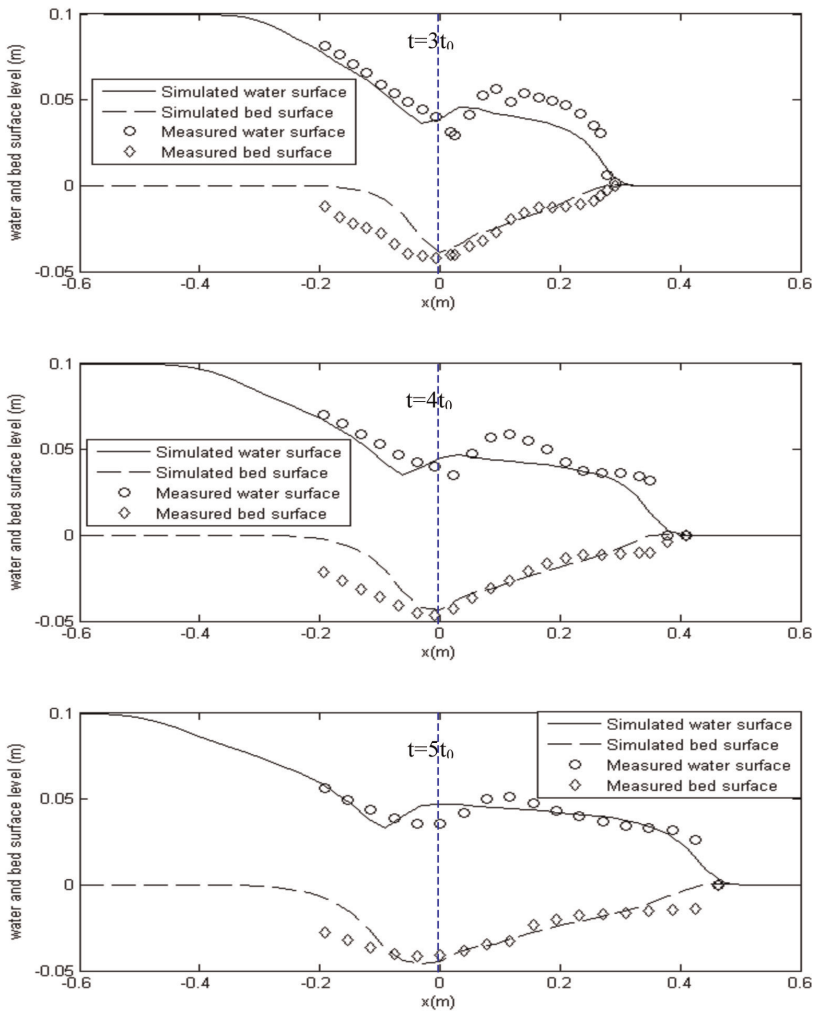

Figure 7. Water and bed surface levels along the centerline in the Taipei experiment ($t_0 = 0.101$ s). The vertical dashed line is the dam location.

Although it was not possible to directly compare the computational resources that these models require because of the unavailability of the codes, it is still useful to note that PIHM_Hydro used 38,208 triangles compared with Yoon and Kang's FV model with nearly 68,000 triangles to achieve a slightly more accurate solution.

[54] The water level, in addition to the arrival time and travel time, is another important criterion for judging

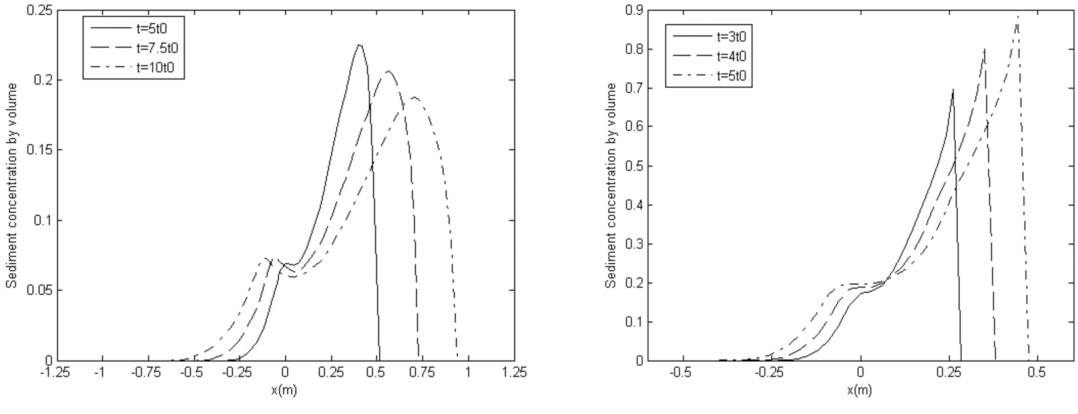

Figure 8. Predicted sediment concentration profiles in the (left) Louvain and (right) Taipei experiments.

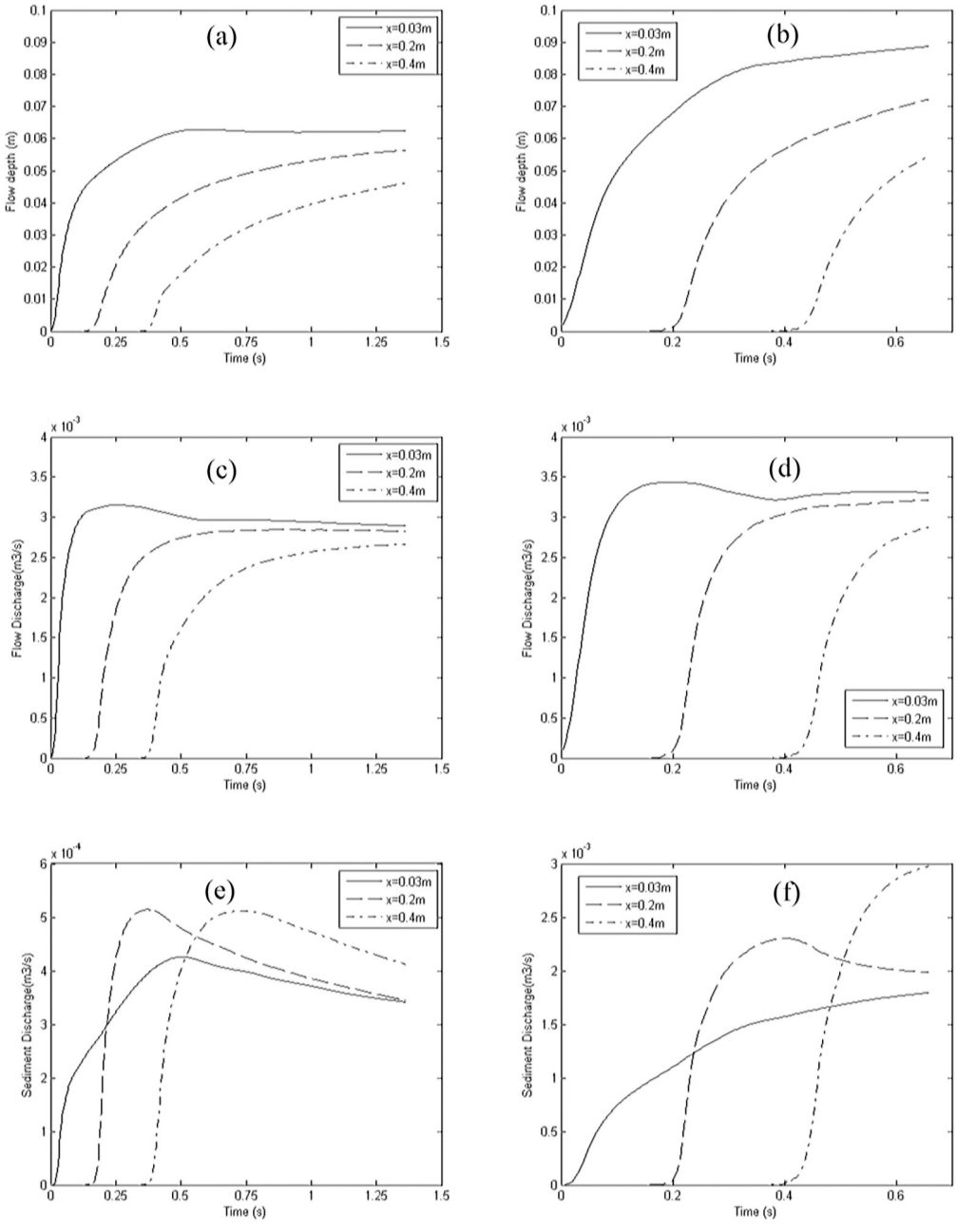

Figure 9. Predicted temporal variations of (a and b) flow depth, (c and d) flow discharge, and (e and f) sediment discharge in the (left) Louvain and (right) Taipei experiments.

whether a model reproduces flow and flood wave phenomena accurately. Table 4 presents comparisons between the predicted and measured maximum water levels. The results are presented in Table 4 for the gauge points along the river and in Table 5 for the police survey points at the left and right banks. As discussed above, the maximum water surface elevations in Table 4 are a better metric to assess model accuracy. According to Table 4, the PIHM_Hydro model produced improved predictions as compared to the finite volume models with smaller RMSEs, while achieving similar accuracy with the commercial finite element model by *Hervouet and Petitjean* [1999]. We note that PIHM_Hydro used far fewer elements than Yoon and Kang's finite volume model. In Tables 4 and 5, we can see that PIHM_Hydro performs very well in terms of stability, accuracy, and robustness on the complicated geometry and topography, even when including the intensive wetting-drying processes which are not included in the other models.

3.5. Case 5. Field-Scale Numerical Experiment With Dam Break and Sediment Dynamics

[55] Finally, case 5 explores a hypothetical 2-D dam break in a wide river reach with a movable bed, previously simulated in 1-D by *Cao et al.* [2004] and *Wu and Wang* [2007]. The channel is 50 km long and 1000 m wide, and the hypothetical dam was initially located at the midpoint

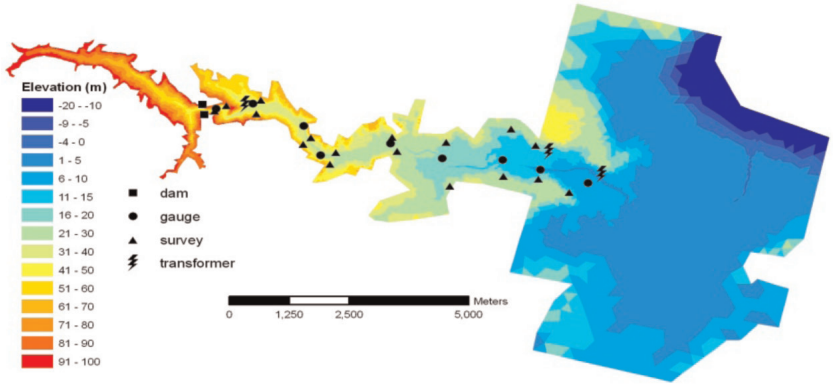

Figure 10. Topography of the Reyran valley and coastal zone for the Malpasset dam break event.

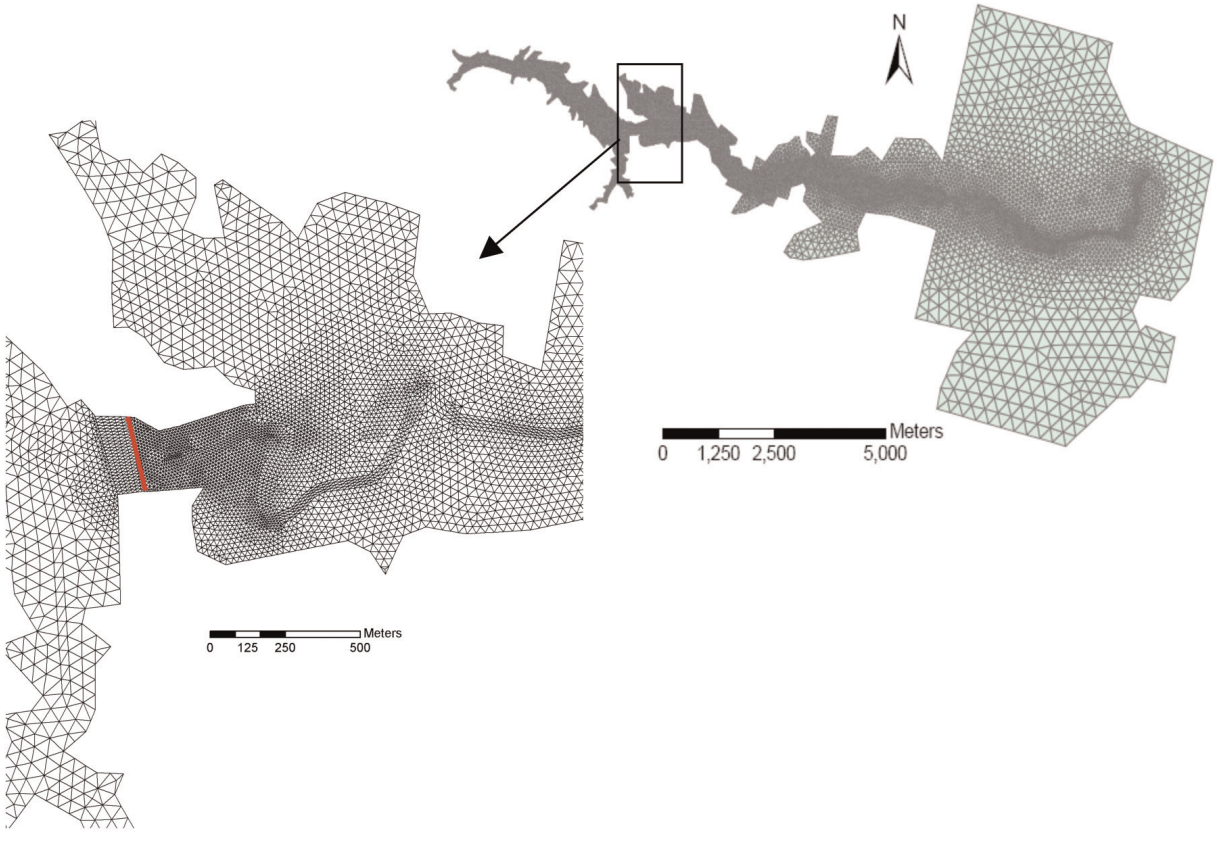

Figure 11. Close-up view of the 38,208-grid mesh near the dam for the Malpasset dam break simulation.

Table 1. Flood Arrival Times at Three Electric Transformers With Different Manning's n on the 26,000-Grid Mesh During Malpasset Dam Break Event

		n (s/m$^{1/3}$)								
Transformer	Measured Time (s)	0.033	0.032	0.031	0.03	0.029	0.028	0.027	0.026	0.025
A	100	130	132	135	139	142	143	144	145	146
B	1240	1225	1209	1191	1174	1156	1137	1119	1100	1079
C	1420	1400	1381	1361	1340	1319	1296	1275	1252	1227

Table 2. Nash-Sutcliffe Efficiency (NSE) and Root-Mean-Square Error (RMSE) of Maximum Water Levels at the Gauge Points and Police Survey Points on Different Spatial Resolutions for the Malpasset Dam Break Event

		Grid Number					
Locations	Metrics	5344	9100	18,533	26,000	38,208	62,549
Gauge	NSE	0.78	0.8	0.81	0.97	0.97	0.97
	RMSE	9.89	9.42	9.22	3.84	3.55	3.52
Police survey	NSE	0.94	0.95	0.96	0.97	0.97	0.98
	RMSE	5.23	5.02	4.14	3.99	3.44	3.19

of the reach. The initial static water depths upstream and downstream from the dam are 40 and 2 m, respectively. Initially, the channel bed is horizontal and is specified to have a noncohesive, uniform sediment with a grain size of 4 mm. The computational domain was discretized to 3329 triangles. The solid wall boundary condition was applied along all boundaries. After *Cao et al.* [2004], we use a value of 0.045 for the critical Shields parameter (θ_c), 0.4 for the bed porosity (p), 2.65 for the specific gravity of sediment particle, and 0.03 s/m$^{1/3}$ for Manning's coefficient (n). The constant α was set at 8.5×10^{-6}.

[56] The 1-D results of *Cao et al.* [2004] and *Wu and Wang* [2007] are compared to PIHM_HYDRO for the

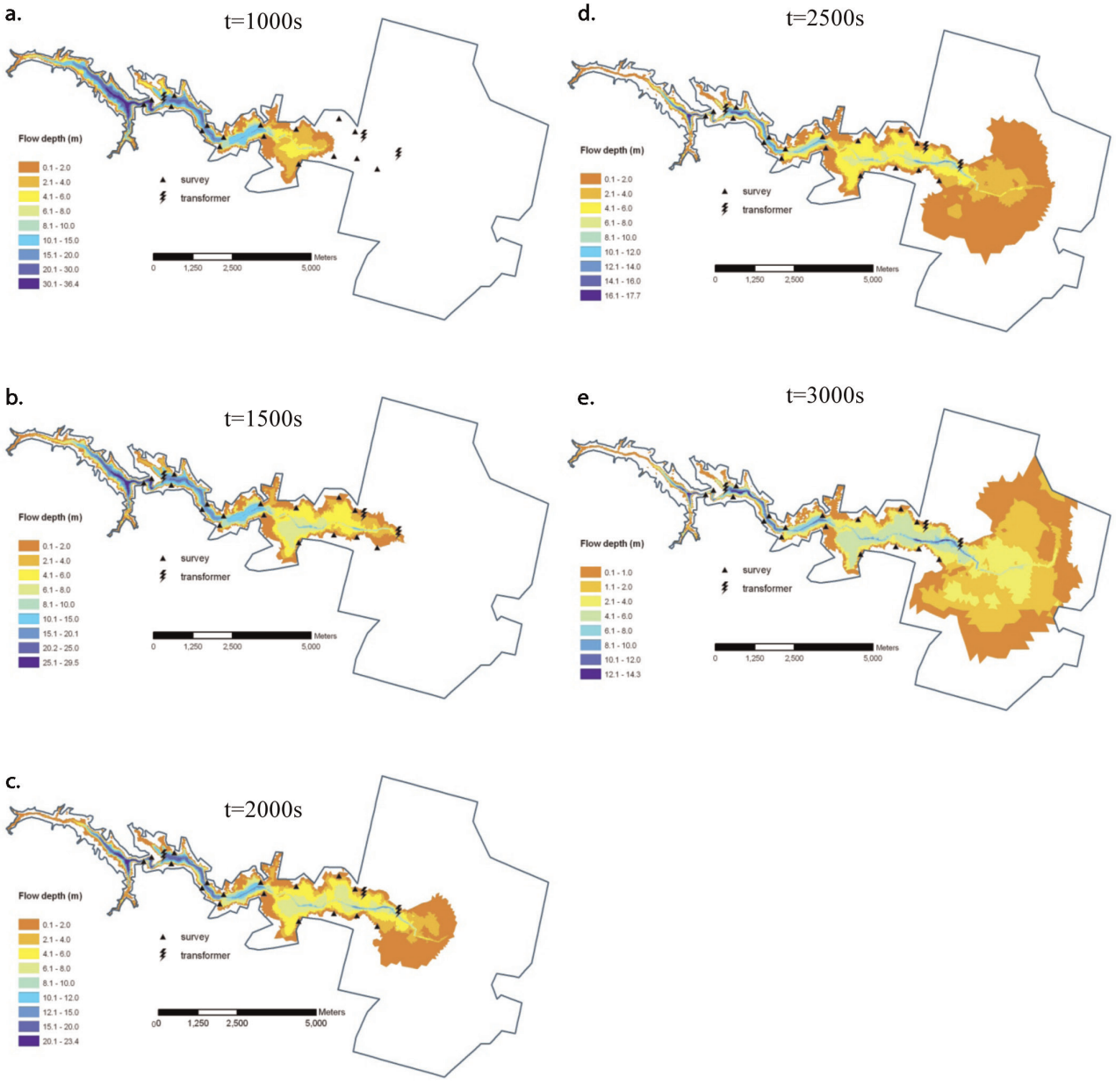

Figure 12. Flood inundation map at different times during the Malpasset dam break event with Manning's $n = 0.033$ s/m$^{1/3}$ on the 38,208-grid mesh.

Table 3. Flood Arrival Times at Three Electric Transformers With Manning's $n = 0.033$ s/m$^{1/3}$ on the 38,208-Grid Mesh During the Malpasset Dam Break Event[a]

	Measured Time (s)	PIHM_Hydro	*Hervouet and Petitjean* [1999]	*Valiani et al.* [2002]	*Yoon and Kang* [2004]
A	100	98 (−2%)	111 (+11%)	98 (−2.0%)	103 (+3.0%)
B	1240	1226 (−1.1%)	1287 (+3.8%)	1305 (+5.2%)	1273 (+2.7%)
C	1420	1402 (− 1.3%)	1436 (+1.1%)	1401 (−1.3%)	1432 (+0.8%)
B−A	1140	1128 (−1.1%)	1176 (+3.2%)	1207 (+5.9%)	1170 (+2.6%)
C−B	180	176 (−2.2%)	149 (−17.2%)	96 (−46.7%)	159 (−11.7%)
Method	N/A	FV	FE	FV	FV
Grid type	N/A	Triangle	Triangle	Quadrilateral	Triangle
Grid number	N/A	38,208	26,000	10,696	67,719

[a]FV and FE denote the finite volume and finite element methods, respectively. B−A is the travel time of the flood wave from transformer A to B, and C−B is for the travel time from transform B to C.

water surface and bed elevation along the centerline of the river reach after the hypothetical dam break (Figure 13). First, we notice that the dam break induces significant erosion. The sediment transport process had a major impact on the flow dynamics, affecting both the water surface profile and wave speed. The results of all three models are similar to the early time results (e.g., $t < 2$ min) from the small-scale experiments discussed in case 3. A hydraulic jump is formed near the dam site because of rapid bed erosion. However, the jump attenuates progressively as it propagates upstream and eventually disappears after about 8 min. Compared to the simulation without sediment transport, the forward wavefront with sediment transport moves more slowly at the early stage, while the backward wave propagates at essentially the same speed. This was also observed by Cao et al. and Wu and Wang. However, after about 20 min, the forward wavefront using equations (13) and (14) propagates at the same speed as without sediment transport, while Cao et al.'s and Wu and Wang's entrainment and deposition solutions propagate much faster.

[57] During the early stage of the dam break, the PIHM_Hydro solution is close to the results of Wu and Wang. At the later time, a large difference develops with respect to the bed surface. In PIHM_HYDRO the erosion and deposition that occur just after the wavefronts passed are not observed in the other models. Cao et al.'s model shows large deposition occurs, while Wu and Wang's model shows attenuated erosion near the wavefront. From Figure 13, it is also noted that only Cao et al.'s equations predict a separate bore upstream of the wavefront. This may be caused by the overprediction of sediment entrainment by Cao et al.'s equations [*Wu and Wang*, 2007].

Table 4. Maximum Water Level at the Gauge Points With Manning's $n = 0.033$ s/m$^{1/3}$ on the 38,208-Grid Mesh During Malpasset Dam Break Event[a]

	Measured Water Level	PIHM_ Hydro	*Hervouet and Petitjean* [1999]	*Valiani et al.* [2002]	*Yoon and Kang* [2004]
6 (Grid point)	84.2	86.48	81.98	88.35	80.85
7 (Grid point)	49.1	53.00	53.86	54.44	55.8
8 (Grid point)	54	53.58	53.8	53.26	53.54
9 (Grid point)	40.2	48.87	48.39	47.93	48.68
10 (Grid point)	34.9	36.99	36.88	36.52	37
11 (Grid point)	27.4	25.01	25.54	25.38	25.7
12 (Grid point)	21.5	18.75	18.48	19.14	19.23
13 (Grid point)	16.1	16.64	17.43	17.66	17.12
14 (Grid point)	12.9	12.79	12.6	12.76	12.86
NSE	0	0.97	0.97	0.97	0.96
RMSE	0	3.55	3.54	3.66	3.97

[a]Values are in meters.

4. Conclusions

[58] This study presents a 2-D high-order model for fully coupled shallow water flow, nonequilibrium sediment transport, and bed evolution (PIHM_Hydro). New formulations were proposed for deposition and erosion. A stable and second-order-accurate numerical algorithm was implemented on unstructured grids using an upwind finite volume method combined with a multidimensional gradient reconstruction and slope limiter technique. A GIS tool is used for automating constrained unstructured domain decomposition from the initial elevation data. The model is capable of producing accurate and stable solutions over a wide range of spatial scales and hydrological events, such as discontinuous flow and the wetting-drying process, by using the approximate Riemann solver and the semi-implicit time integration technique based on CVODE [*Cohen and Hindmarsh*, 1994].

Table 5. Maximum Water Level at the Police Survey Points With Manning's $n = 0.033$ s/m$^{1/3}$ on the 38,208-Grid Mesh During the Malpasset Dam Break Event[a]

	Measured Water Level	PIHM_Hydro	*Valiani et al.* [2002]	*Yoon and Kang* [2004]
1 (Survey point)	79.15	81.01	75.96	75.13
2 (Survey point)	87.2	90.04	89.34	87.38
3 (Survey point)	54.9	52.90	53.77	55.09
4 (Survey point)	64.7	56.83	59.64	57.41
5 (Survey point)	51.1	46.75	45.56	47.11
6 (Survey point)	43.75	43.89	44.85	45.74
7 (Survey point)	44.35	42.41	42.86	40.47
8 (Survey point)	38.6	31.84	34.61	32.58
9 (Survey point)	31.9	32.71	32.44	33.16
10 (Survey point)	40.75	37.39	38.12	38.29
11 (Survey point)	24.15	23.57	25.37	25.16
12 (Survey point)	24.9	28.06	27.35	25.96
13 (Survey point)	17.25	21.82	23.58	24.41
14 (Survey point)	20.7	21.42	23.19	20.58
15 (Survey point)	18.6	19.43	19.37	19.08
16 (Survey point)	17.25	20.13	20.39	17.04
17 (Survey point)	14	15.66	14.23	16
NSE	0	0.97	0.98	0.97
RMSE	0	3.44	3.10	3.48

[a]Values are in meters.

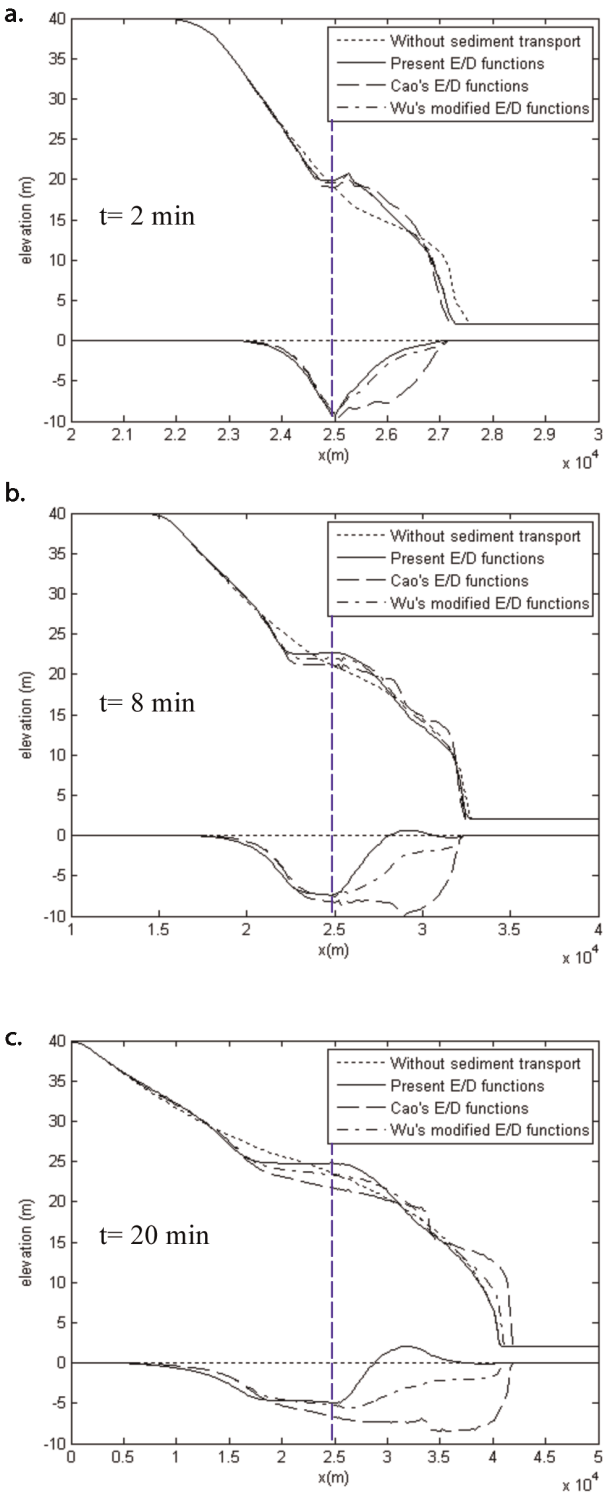

Figure 13. Predicted water and bed surface levels along the centerline in the field-scale-wide river test case. The blue line represents the dam site.

[59] PIHM_HYDRO is compared to laboratory- and field-scale experiments, as well as other models with comparable physics from the literature and the results. For the laboratory-scale Bellos experiment (case 1), the model was able to accurately simulate the wetting-drying process and supercritical flow. In case 2, the rainfall-runoff experiment maintains a mass-conserving solution for rapid wetting-drying surfaces. In case 3, we examine a laboratory-scale experiment which demonstrates the interaction of flow and sediment transport following a dam break. Case 3 demonstrates that (1) the hydraulic jump, which forms below the dam break because of rapid bed erosion, propagates upstream and (2) extremely high sediment concentrations within the dam break wavefront leads to sharp forefronts of the sediment

concentration profile. In case 4 the model was applied to the real dam break and flood event, the Malpasset dam accident, with complex topography and geometry as well as discontinuous rapid flow and wetting-drying processes. The model was found to have excellent agreement with measurements, including the arrival times, travel times of the flood wave, the maximum water surface along the river and the banks, and the boundary of flooded area. For case 5, it was found that after a long time relative to the wavefront duration (e.g., 20 min in the large river case), deposition occurs as a trailing wave of very high sediment concentration in the water column, which was not observed in the other models studied here. It shows that fully coupled 2-D sediment transport and bed erosion have a major impact on the flow dynamics, affecting both the water surface profile and wave speed of model solutions. PIHM_HYDRO is an open source code and is freely available with all test cases described here for community access at http://www.pihm.psu.edu.

Appendix A

[60] To evaluate the flux using an approximate Riemann solver, the Jacobian of the normal flux ($\mathbf{F} \times \mathbf{n}$) is calculated.

$$\mathbf{J}_n = \begin{pmatrix} 0 & n_x & n_y & 0 & 0 \\ (c^2-u^2)n_x - uvn_y & 2un_x + vn_y & un_y & 0 & 0 \\ -uvn_x + (c^2-v^2)n_y & vn_x & un_x + 2vn_y & 0 & 0 \\ -(un_x+vn_y)\psi & \psi n_x & \psi n_y & un_x+vn_y & 0 \\ -(un_x+vn_y)\psi & \psi n_x & \psi n_x & un_x+vn_y & 0 \end{pmatrix}, \tag{A1}$$

where $\mathbf{J}_n = \frac{\partial(\mathbf{F}\times\mathbf{n})}{\partial \mathbf{U}} = \frac{\partial(\mathbf{E})}{\partial \mathbf{U}} n_x + \frac{\partial(\mathbf{G})}{\partial \mathbf{U}} n_y$. The eigenvalues are

$$\lambda_1 = un_x + vn_y + c, \lambda_2 = un_x + vn_y, \lambda_3 = un_x + vn_y - c, \lambda_4 = un_x + vn_y, \lambda_5 = 0, \tag{A2}$$

with $c = \sqrt{gh}$ being the celerity of small-amplitude gravitational waves. Corresponding eigenvectors are given by

$$\mathbf{e}_1 = \begin{pmatrix} 1 \\ u + n_x c \\ v + n_y c \\ c \\ c \end{pmatrix}, \mathbf{e}_2 = \begin{pmatrix} 0 \\ -n_y \\ n_x \\ 0 \\ 0 \end{pmatrix}, \mathbf{e}_3 = \begin{pmatrix} 1 \\ u - n_x c \\ v - n_y c \\ c \\ c \end{pmatrix}, \mathbf{e}_4 = \begin{pmatrix} 0 \\ 0 \\ 0 \\ 1 \\ 1 \end{pmatrix}, \mathbf{e}_5 = \begin{pmatrix} 0 \\ 0 \\ 0 \\ 0 \\ 1 \end{pmatrix}. \tag{A3}$$

[61] This hyperbolic system is degenerate since one eigenvalue is zero. It has two shocks, two rarefaction waves, or a shock plus a rarefaction wave in addition to a contact discontinuity. The contact discontinuity is produced on the basis of the assumption of negligible flow turbulence and sediment diffusion [see *Toro*, 2001; *Fagherazzi and Sun*, 2003].

[62] Several formulations for the numerical flux at the boundary of two elements were found to be satisfactory [*Toro*, 2001], but Roe's formulation was consistently more stable, producing solutions at extreme conditions where others fail [*Sleigh et al.*, 1998].

[63] The numerical flux is given by

$$\mathbf{F}_n = \frac{1}{2}\left[\mathbf{F}(\mathbf{U}_L)\times\mathbf{n} + \mathbf{F}(\mathbf{U}_R)\times\mathbf{n} - \left|\tilde{\mathbf{J}}_n\right|(\mathbf{U}_R - \mathbf{U}_L)\right], \tag{A4}$$

where $\mathbf{U}_L$ and $\mathbf{U}_R$ are the left and right conserved variables and $\tilde{\mathbf{J}}_n$ is the modified Jacobian with a form similar to $\mathbf{J}_n$ and must meet the following requirements [*Roe*, 1981].

[64] 1. $\tilde{\mathbf{J}}_n$ depends on the left and right states.

[65] 2. $\tilde{\mathbf{J}}_n$ is diagonalizable with real eigenvalues and a set of eigenvectors.

[66] 3. $(\mathbf{F}\times\mathbf{n})_R - (\mathbf{F}\times\mathbf{n})_L = \tilde{\mathbf{J}}_n(\mathbf{U}_R - \mathbf{U}_L)$.

[67] 4. $\tilde{\mathbf{J}}_n \to \mathbf{J}_n(\tilde{\mathbf{U}})$ as $\mathbf{U}_L, \mathbf{U}_R \to \mathbf{U}$.

[68] $\tilde{\mathbf{J}}_n$ can be evaluated as $\tilde{\mathbf{J}}_n = \mathbf{J}_n(\tilde{\mathbf{U}})$ with $\tilde{\mathbf{U}}$ being some average values based on the left and right states. A change of variable is used to find the Jacobian matrix meeting these requirements [*Roe*, 1981; *LeVeque*, 2002]. It is noted that the bottom elevation is always continuous at the shock and contact discontinuity locations according to the Rankine-Hugoniot conditions [*Fagherazzi and Sun*, 2003]. The intermediate states are calculated as

$$\tilde{h} = \frac{h_L + h_R}{2}, \tilde{u} = \frac{u_L\sqrt{h_L} + u_R\sqrt{h_R}}{\sqrt{h_L}+\sqrt{h_R}}, \tilde{v} = \frac{v_L\sqrt{h_L} + v_R\sqrt{h_R}}{\sqrt{h_L}+\sqrt{h_R}}, \tilde{\psi} = \frac{\psi_L\sqrt{h_L} + \psi_R\sqrt{h_R}}{\sqrt{h_L}+\sqrt{h_R}}. \tag{A5}$$

[69] The eigenvalues of $\tilde{\mathbf{J}}_n$ are given by

$$\tilde{\lambda}_1 = \tilde{u}n_x + \tilde{v}n_y + \tilde{c}, \tilde{\lambda}_2 = \tilde{u}n_x + \tilde{v}n_y, \tilde{\lambda}_3 = \tilde{u}n_x + \tilde{v}n_y - \tilde{c}, \tilde{\lambda}_4 + \tilde{u}n_x + \tilde{v}n_y, \tilde{\lambda}_5 = 0, \tag{A6}$$

with $\tilde{c} = \sqrt{g\tilde{h}}$, and the corresponding eigenvectors are

$$\tilde{\mathbf{e}}_1 = \begin{pmatrix} 1 \\ \tilde{u} + n_x\tilde{c} \\ \tilde{v} + n_y\tilde{c} \\ \tilde{\psi} \\ \tilde{\psi} \end{pmatrix}, \tilde{\mathbf{e}}_2 = \begin{pmatrix} 0 \\ -n_y \\ n_x \\ 0 \\ 0 \end{pmatrix}, \tilde{\mathbf{e}}_3 = \begin{pmatrix} 1 \\ \tilde{u} - n_x\tilde{c} \\ \tilde{v} - n_y\tilde{c} \\ \tilde{\psi} \\ \tilde{\psi} \end{pmatrix}, \tilde{\mathbf{e}}_4 = \begin{pmatrix} 0 \\ 0 \\ 0 \\ 1 \\ 1 \end{pmatrix}, \tilde{\mathbf{e}}_5 = \begin{pmatrix} 0 \\ 0 \\ 0 \\ 0 \\ 1 \end{pmatrix}. \tag{A7}$$

[70] The difference in the left and right conserved variables can be expressed as Jacobian eigenvectors:

$$d\mathbf{U} = \mathbf{U}_R - \mathbf{U}_L = \sum_{k=1}^{5} \alpha_k \tilde{e}_k \tag{A8}$$

with

$$\alpha_1 = \frac{(h_R - h_L)}{2} + \frac{\left\{\left[(hu)_R - (hu)_L\right]n_x + \left[(hv)_R - (hv)_L\right]n_y - (h_R - h_L)\left(\tilde{u}n_x + \tilde{v}n_y\right)\right\}}{2\tilde{c}},$$
$$\alpha_2 = \left[(hu)_R - (hu)_L - (h_R - h_L)\tilde{v}\right]n_x - \left[(hu)_R - (hu)_L - (h_R - h_L)\tilde{u}\right]n_y, \tag{A9}$$
$$\alpha_3 = \frac{(h_R - h_L)}{2} - \frac{\left\{\left[(hu)_R - (hu)_L\right]n_x + \left[(hv)_R - (hv)_L\right]n_y - (h_R - h_L)\left(\tilde{u}n_x + \tilde{v}n_y\right)\right\}}{2\tilde{c}},$$

$$\alpha_4(h\psi)_R - (h\psi)_L - (h_R - h_L)\tilde{\psi}$$

$$\alpha_5(\varphi_R - \varphi_L) - \left((h\varphi)_R - (h\varphi)_L\right)$$

[71] Therefore, $\left|\tilde{\mathbf{J}}_n\right|(\mathbf{U}_R - \mathbf{U}_L) = \sum_{k=1}^{5} \left|\tilde{\lambda}_k\right|\alpha_k\tilde{\mathbf{e}}_k$, and the numerical flux is calculated as

$$\mathbf{F}_n = \frac{1}{2}\left[\mathbf{F}(\mathbf{U}_L)\times\mathbf{n} + \mathbf{F}(\mathbf{U}_R)\times\mathbf{n} - \sum_{k=1}^{5}\left|\tilde{\lambda}_k\right|\alpha_k\tilde{\mathbf{e}}_k\right]. \tag{A10}$$

[72] To avoid entropy violation at the sonic point or critical flow condition, a fix proposed by *Harten and Hyman* [1983] is incorporated:

$$\left|\tilde{\lambda}_k\right| = \begin{cases} \left|\tilde{\lambda}_k\right| & \text{if} \left|\tilde{\lambda}_k\right| \geq \delta, \\ \delta & \text{if} \left|\tilde{\lambda}_k\right| < \delta. \end{cases} \tag{A11}$$

$$\delta = \max\left[0, \tilde{\lambda}_k - (\lambda_k)_L, (\lambda_k)_R - \tilde{\lambda}_k\right]. \tag{A12}$$

[73] **Acknowledgments.** This research was funded by grants from the National Science Foundation, EAR 0725019 Shale Hills-Susquehanna Critical Zone Observatory, EAR 0609791 A Synthesis of Community Data and Modeling for Advancing River Basin Science: The Susquehanna.

References

Abbott, M. B., J. A. Bathurst, and P. E. Cunge (1986), An introduction to the European Hydrological System-Systeme Hydrologicque Europeen "SHE" 2: Structure of a physically based distributed modeling system, *J. Hydrol.*, *87*, 61–77.

Aizinger, V., and C. Dawson (2002), A discontinuous Galerkin method for two-dimensional flow and transport in shallow water, *Adv. Water Resour.*, *25*, 67–84.

Alcrudo, F., and P. Garcia-Navarro (1993), A high-resolution Godunov-type scheme in finite volumes for the 2D shallow-water equations, *Int. J. Numer. Methods Fluids*, *16*, 489–505.

Ambrosi, D. (1995), Approximation of shallow water equations by Roe's Riemann solver, *Int. J. Numer. Methods Fluids*, *20*, 157–168.

Anastasiou, K. and C. T. Chan (1997), Solution of the 2D shallow water equations using the finite volume method on unstructured triangular meshes, *Int. J. Numer. Methods Fluids*, *24*, 1225–1245.

Begnudelli, L., and B. F. Sanders (2006), Unstructured grid finite volume algorithm for shallow-water flow and scalar transport with wetting and drying, *J. Hydraul. Eng.*, *132*, 371–384.

Bellos, C., and V. Hrissanthou (1998), Numerical simulation of sediment transport following a dam break, *Water Resour. Manage.*, *12*, 397–407.

Bellos, C. V., J. V. Soulis, and J. G. Sakkas (1992), Experimental investigation of two-dimensional dam-break induced flows, *J. Hydraul. Res.*, *30*, 47–63.

Bennett, J. P. (1974), Concepts of mathematical modeling of sediment yield, *Water Resour. Res.*, *10*, 485–492.

Bhatt, G., M. Kumar, and C. J. Duffy (2008), Bridging gap between geohydrologic data and Integrated Hydrologic Model: PIHMgis, paper presented at iEMSs 2008 International Congress on Environmental Modelling and Software, Barcelona.

Bradford, S. F., and B. F. Sanders (2002), Finite-volume model for shallow-water flooding of arbitrary topography, *J. Hydraul. Eng.*, *128*, 289–298.

Caleffi, V., A. Valiani, and A. Zanni (2003), Finite volume method for simulating extreme flood events in natural channels, *J. Hydraul. Res.*, *41*, 167–177.

Cao, Z., G. Pender, S. Wallis, and P. Carling (2004), Computational dam-break hydraulics over erodible sediment bed, *J. Hydraul. Eng.*, *130*, 689–703.

Capart, H., and D. L. Young (1998), Formation of a jump by the dam-break wave over a granular bed, *J. Fluid Mech.*, *372*, 165–187.

Castro Diaz, M. J., E. D. Fernandez-Nieto, and A. M. Ferreiro (2008), Sediment transport models in shallow water equations and numerical approach by high order finite volume methods, *Comput. Fluids*, *37*, 299–316.

Cohen, S. D., and A. C. Hindmarsh (1994), CVODE user guide, *Tech. Rep. UCRL-MA-118618*, Lawrence Livermore Natl. Lab., Berkeley, Calif.

diGiammarco, P., E. Todini, and P. Lamberti (1996), A conservative finite elements approach to overland flow: The control volume finite element formulation, *J. Hydrol.*, *175*, 267–291.

Fagherazzi, S., and T. Sun (2003), Numerical simulations of transportation cyclic steps, *Comput. Geosci.*, *29*, 1143–1154.

Fennema, R. J., and M. H. Chaudhry (1990), Explicit methods for 2D transient free-surface flows, *J. Hydraul. Eng.*, *116*, 1013–1034.

Fraccarollo, L., and H. Capart (2002), Riemann wave description of erosional dam-break flows, *J. Fluid Mech.*, *461*, 183–228.

Fraccarollo, L., H. Capart, and Y. Zech (2003), A Godunov method for the computation of erosional shallow water transients, *Int. J. Numer. Methods Fluids*, *41*, 951–976.

Goutal, N. (1999), The Malpasset dam failure—An overview and test case definition, paper presented at the 4th CADAM meeting, CADAM, Zaragoza, Spain, 18–19 Nov.

Harten, A., and J. M. Hyman (1983), Self-adjusting grid for one dimensional hyperbolic conservation laws, *J. Comput. Phys.*, *50*, 235–269.

Henderson, F. M. (1966), *Open Channel Flow*, MacMillan, New York.

Hervouet, J. M. (2000), A high resolution 2-D dam-break model using parallelization, *Hydrol. Processes*, *14*, 2211–2230.

Hervouet, J. M., and A. Petitjean (1999), Malpasset dam-break revisited with two-dimensional computations, *J. Hydraul. Res.*, *37*, 777–788.

Hindmarsh, A. C., and R. Serban (2005), User documentation for CVODE v2.3.0, *Rep. UCRL-SM-208108*, Cent. for Appl. Sci. Comput., Lawrence Livermore Natl. Lab., Berkeley, Calif.

Hubbard, M. E. (1999), Multidimensional slope limiters for MUSCL-type finite volume schemes on unstructured grids, *J. Comput. Phys.*, *155*, 54–74.

Hudson, J., and P. K. Sweby (2003), Formulations for numerically approximating hyperbolic systems governing sediment transport, *J. Sci. Comput.*, *19*, 225–252.

Hudson, J., and P. K. Sweby (2005), A high-resolution scheme for the equations governing 2D bed-load sediment transport, *Int. J. Numer. Methods Fluids*, *47*, 1085–1091.

Jawahar, P., and H. Kamath (2000), A high-resolution procedure for Euler and Navier-Stokes computations on unstructured grids, *J. Comput. Phys.*, *164*, 165–203.

Katopodes, N., and T. Strelkoff (1978), Computing two-dimensional dam-break flood waves, *J. Hydraul. Div. Am. Soc. Civ. Eng.*, *104*, 1269–1288.

Kumar, M., G. Bhatt, and C. J. Duffy (2008), An efficient domain decomposition framework for accurate representation of geodata in distributed hydrologic models, *Int. J. Geogr. Inf. Sci.*, *23*, 1569–1596.

LeVeque, R. J. (2002), *Finite Volume Methods forHyperbolic Problems*, 535 pp., Cambridge Univ. Press, Cambridge, Mass.

Liu, X., B. J. Landry, and M. H. García (2008), Two-dimensional scour simulations based on coupled model of shallow water equations and sediment transport on unstructured meshes, *Coastal Eng.*, *55*, 800–810.

Loukili, Y., and A. Soulaimani (2007), Numerical tracking of shallow water waves by the unstructured finite volume WAF approximation, *Int. J. Comput. Methods Eng.*, *8*, 75–88.

Martin, N., and S. M. Gorelick (2005), A MATLAB surface fluid flow model for rivers and streams, *Comput. Geosci.*, *31*, 929–946.

Molls, T., and M. H. Chaudhry (1995), Depth averaged open channel flow model, *J. Hydraul. Eng.*, *121*, 453–465.

Nash, J. E., and J. V. Sutcliffe (1970), River flow forecasting through conceptual models part I—A discussion of principles, *J. Hydrol.*, *10*, 282–290.

Ottevanger, W. (2005), Discontinuous finite element modeling of river hydraulics and morphology, M.S. thesis, Univ. of Twente, Enschede, Netherlands.

Panday, S., and P. Huyakorn (2004), A fully-coupled physically-based spatially distributed model for evaluating surface/subsurface flow, *Adv. in Water Resour.*, *27*, 361–382.

Qu, Y., and C. J. Duffy (2007), A semidiscrete finite volume formulation for multiprocess watershed simulation, *Water Resour. Res.*, *43*, W08419, doi:10.1029/2006WR005752.

Roache, P. J. (1994), Perspective: A method for uniform reporting of grid refinement studies, *J. Fluids Eng.*, *116*, 405–413.

Roe, P. L. (1981), Approximate Riemann solvers, parameter vectors, and difference schemes, *J. Comput. Phys.*, *43*, 357–372.

Rosatti, G., and L. Fraccarollo (2006), A well-balanced approach for flows over mobile-bed with high sediment-transport, *J. Comput. Phys.*, *220*, 312–338.

Shewchuk, J. R. (1997), Delaunay refinement mesh generation, Ph.D. thesis, Carnegie Mellon Univ., Pittsburgh, Pa.

Shu, C. W., and S. Osher (1988), Efficient implementation of essentially non-oscillatory shock capturing schemes, *J. Comput. Phys.*, *77*, 439–471.

Simpson, G., and S. Castelltort (2006), Coupled model of surface water flow, sediment transport and morphological evolution, *Comput. Geosci.*, *32*, 1600–1614.

Sleigh, P. A., M. Berzins, P. H. Gaskell, and N. G. Wright (1998), An unstructured finite-volume algorithm for predicting flow in rivers and estuaries, *Comput. Fluids*, *27*, 479–508.

Soares Frazão, S., F. Alcrudo, and N. Goutal (1999), Dam-break test cases summary, paper presented at 4th CADAM Meeting, CADAM, Zaragoza, Spain, 18–19 Nov.

Toro, E. F. (1999), *Riemann Solvers and Numerical Methods for Fluid Dynamics*, Springer, New York.

Toro, E. F. (2001), *Shock-Capturing Methods for Free-Surface Shallow Flows*, John Wiley, Chichester, U. K.

Valiani, A., V. Caleffi, and A. Zanni (2002), Case study: Malpasset dam-break simulation using a two-dimensional finite volume method, *J. Hydraul. Eng.*, *128*, 460–472.

VanderKwaak, J. (1999), Numerical simulation of flow and chemical transport in integrated surface-subsurface hydrologic systems, Ph.D. thesis in Earth Sciences, Univ. of Waterloo, Waterloo, Ont., Canada.

Wang, J. W., and R. X. Liu (2000), A comparative study of finite volume methods on unstructured meshes for simulation of 2D shallow water wave problems, *Math. Comput. Simul.*, *53*, 171–184.

Wu, W., and S. Wang (2007), One-dimensional modeling of dam-break flow over movable beds, *J. Hydraul. Eng.*, *133*, 48–58.

Yoon, T. H., and S. K. Kang (2004), Finite volume model for two-dimensional shallow water flows on unstructured grids, *J. Hydraul. Eng.*, *130*, 678–688.

Zhao, D. H., H. W. Shen, G. Q. Tabios III, J. S. Lai, and W. Y. Tan (1994), Finite-volume two-dimensional unsteady-flow model for river basins, *J. Hydraul. Eng.*, *120*, 863–883.

C. J. Duffy and S. Li, Department of Civil and Environmental Engineering, Pennsylvania State University, 212 Sackett Bldg., University Park, PA 16802, USA. (cxd11@psu.edu)